

# Improving convergence of volume penalized fluid-solid interactions

Eric W. Hester <sup>\*</sup>      Geoffrey M. Vasil <sup>\*</sup>      Keaton J. Burns <sup>†‡</sup>

April 30, 2022

## Abstract

Boundary conditions on arbitrary geometries are a common issue in simulating partial differential equations. The conventional approach is to discretize on a grid conforming to the geometry. However grid construction is challenging, and this difficulty is compounded for evolving domains. Several methods instead augment the equations themselves to implicitly enforce the boundary conditions. This paper examines the Volume Penalty Method, which approximates Dirichlet boundary conditions in the Navier Stokes equations with rapid linear damping (non-dimensional time scale  $\eta$ ) inside the object. This technique is proven to converge to the true solution, and also leads to simple volume-integral force and torque calculations. Unfortunately, previous analysis showed convergence of only  $\mathcal{O}(\eta^{1/2})$ . We analyze the source of this error using matched asymptotic expansions and show that it stems from a displacement length, proportional to a Reynolds number  $Re$  dependent boundary layer of size  $\mathcal{O}(\eta^{1/2} Re^{-1/2})$ . The relative size of the displacement length and damping time scale lead to the emergence of multiple asymptotic regimes. The key finding is that there is a simple correction that can be efficiently calculated to eliminate the displacement length and promote the accuracy to  $\mathcal{O}(\eta)$ . This improvement also extends to the force and torque calculations. We demonstrate these findings in 1D planar Poiseuille flow, 2D steady flow past a viscous stagnation point, and 2D unsteady flow past a rotating cylinder, and finally show that Richardson extrapolation can be used with our correction to further improve convergence to  $\mathcal{O}(\eta^2)$ .

## 1 Introduction

### 1.1 Arbitrary geometry boundary conditions

Partial Differential Equations are used to model many important phenomena in fundamental and applied science, engineering, and industry. Fluid dynamics, elastodynamics, electromagnetism, melting, dissolution, and erosion are all understood in terms of canonical PDEs. Many relevant problems concern complicated geometries which may also evolve in time. Such problems are often modelled mathematically with different PDEs on distinct domains, and boundary conditions applied at the interfaces. They can then be simulated by discretizing on numerical grids which conform to the given geometry. These grids must be updated if the geometry changes over time, leading to significant difficulties, particularly for topological changes observed in many phenomena.

---

<sup>\*</sup>University of Sydney School of Mathematics and Statistics, Sydney, NSW 2006, Australia (eric.hester@sydney.edu.au).

<sup>†</sup>Massachusetts Institute of Technology Department of Physics, Cambridge, MA 02139, USA

<sup>‡</sup>Center for Computational Astrophysics, Flatiron Institute, Simons Foundation, New York, NY 10010, USA

This approach, while ubiquitous, is in fact an idealization. Reality is smooth. While many thermodynamical phenomena were first modelled as arising from material discontinuities (Gibbs’ analysis of capillary forces [16], or Stefan’s melting phase transitions [36]), it was eventually appreciated that these effects are more accurately modelled as possessing small but finite length scales (Van der Waals’ explanation of surface tension [38], and Cahn and Hilliard’s model of phase separation [9]). What appear to be boundary conditions on a lower dimensional manifold are often small scale regularised transitions which emerge from microphysics we have omitted in the model. For example, the addition of vanishing diffusion to Burgers equation allows the regularization of shock discontinuities [11, 19] and leads directly to the classical Rankine-Hugoniot jump conditions). In essence, many classical discontinuous boundary conditions only arise as an infinitesimal limit to physical phenomena with finite thickness.

Many numerical methods adopt this philosophy of smoothness and exploit it to achieve greater numerical simplicity, efficiency, and generality. Instead of simulating a reduced PDE on an arbitrary (possibly evolving) geometry with complicated discretization, one *augments the equations*; A single set of PDEs applies over all subdomains, which implicitly reproduce the desired boundary conditions between disparate regions. A successful example of this is the phase field technique, a series of partial differential equations used to model quite general phase transition phenomena. Originally derived from thermodynamical considerations of free energy [18], the phase field method can also be derived purely as a regularised system to reproduce desired discontinuous boundary conditions [27]. The parameters included in the model are flexible enough to admit several asymptotic regimes, which reduce to multiple classical multi-phase models in the limit, such as Stefan boundary conditions, with or without surface tension or kinetic effects, mean curvature flow, or the Cahn-Hilliard equation itself [8]. However this asymptotic convergence is often proportional to boundary layer thickness, which is orders of magnitude larger in simulations than in nature – appearing to discredit the usefulness of a diffuse approach. Fortunately, a detailed understanding of the structure of the boundary layer can reveal distinguished limits which allow improved convergence of the method [23, 12] vastly improving the accuracy of these models.

The diffuse domain method was similarly developed as a smoothed means to approximate Neumann, Robin, and Dirichlet boundary conditions [29, 15, 28, 7].

An area of particular interest has been applying such methods to fluid dynamics. Phase field approaches to multi-phase mixtures have been developed [21], along with more general diffuse interface methods [2]. However, fluid-structure interaction can be difficult to model using phase field approaches derived for multi-phase fluids. The classical approach is Peskin’s immersed boundary method [32, 33], which smoothly interpolates the reciprocal forces of the fluid and the flexible elastic structure via convolutions with regularized delta functions. A struggle for this approach is dealing with rigid boundaries, for which the stiffness of the elastic object becomes numerically challenging [31].

An alternative approach to modelling rigid objects within fluid flows is the volume penalty method. This simple method has origins in rather general forcing approaches [6, 17]. Much as for the phase field method, this approach also has a physical motivation, in terms of flow through a porous medium [3, 4]. The versatility of the method has spawned subsequent applications to simulations of Navier Stokes with arbitrary geometries [25, 24, 20, 39], moving boundaries [31, 26], magnetohydrodynamics [35], no-flux boundary conditions [22], and even insect flight [13, 14].

The Volume Penalty method approximates Dirichlet boundary conditions with strong linear damping within the interior of the boundary (hence *volume* penalization), and is parameterized by a damping timescale

$$\text{Damping timescale} = \tau. \tag{1}$$

It has been proven that the true solution is attained in the limit that the damping timescale  $\tau$  tends to zero [3]. This is conventionally done using discontinuous damping coincident with interior of the desired boundary. However, this approach has two significant drawbacks. The error of the method scales as  $\mathcal{O}(\tau^{1/2})$  [10], leading to slow convergence. Additionally, discontinuous damping impacts numerical convergence in many methods (for instance, causing Gibbs phenomena in pseudospectral codes [24]).

## 1.2 Paper overview

The aim of this paper is to thoroughly investigate the source of error of the volume penalty method. The outline is as follows.

- Section 2 defines the key concepts of our investigation. The standard approach for rigid no-slip boundaries in incompressible hydrodynamics is reviewed, including the standard force calculation  $F_0$  and torque calculation  $T_0$ . We then describe the volume penalty method, along with the new drag calculation  $F$  and torque calculation  $T$ , and define the key non-dimensional parameters of *Reynolds number*  $\text{Re}$ , *damping time scale*  $\eta$  and *damping length scale*  $\varepsilon = \sqrt{\eta/\text{Re}}$ . We also remark how the mathematical convergence relates to the numerical convergence of the method. We then define our error metrics of *global error*  $\mathcal{E}_1$ , *local error*  $\mathcal{E}_\infty$ , and *drag and torque error*  $\Delta F, \Delta T$ , and the central concept of *displacement length*  $\ell^*$ . We finally define the class of *mask functions*  $\Gamma$ , give representative examples, and the *shifting*  $\ell$  and *smoothing*  $\delta$  transformations we apply near the boundary.
- Section 3 develops the vector calculus needed to understand fluid dynamics in the boundary layer around an arbitrary object. This is achieved by using a *signed distance function*  $\sigma$  coordinate system. We first discuss vector calculus on the boundary (the tangent space to the manifold). We then examine the normal to the boundary  $\hat{n}$  (the normal vector bundle), and finally develop all required vector calculus operators.
- Section 4 analyzes the volume penalty method for incompressible hydrodynamics around an arbitrary smooth object using multiple scales matched asymptotics. We separate the problem into fluid  $\Omega^+$ , solid  $\Omega^-$ , and boundary  $\Delta\Omega$  regions. Asymptotic expansions in  $\varepsilon$  are applied in each region, with  $\varepsilon$  rescaling in the boundary layer. We enforce asymptotic matching conditions between adjacent layers. The leading order problem justifies the convergence of the volume penalty method to an ideal no-slip boundary. The first order correction shows general masks  $\Gamma$  lead to an  $\mathcal{O}(\varepsilon)$  displacement length error in the velocity and pressure in the fluid region. However,  $\mathcal{O}(\varepsilon)$  mask corrections can eliminate the displacement length, localize the flow error to the  $\mathcal{O}(\varepsilon)$  boundary region, and achieve  $\mathcal{O}(\varepsilon^2)$  accuracy in the fluid. The second order asymptotics gives rise to two asymptotic error regimes: Large damping ( $1 > \text{Re}^{-1} > \varepsilon > \eta$ ) implies the first order displacement length error  $\mathcal{O}(\varepsilon)$  dominates the second order time scale error  $\mathcal{O}(\eta) = \mathcal{O}(\text{Re} \varepsilon^2)$ , and convergence can only be improved to  $\mathcal{O}(\eta)$  accuracy using our mask corrections. Intermediate damping ( $1 > \eta > \varepsilon > \text{Re}^{-1}$ ) reverses the ordering, explaining temporarily heightened convergences for previous experimental results at high  $\text{Re}$  [4]. We analyze the computational costs in these different regimes by comparing the damping time and length scales to the turbulent Kolmogorov length scale and CFL time scale. We finally show how improved flow accuracy also extends to the force and torque calculations.
- Section 5 develops a constructive approach to optimizing mask functions. The traditional discontinuous mask gives an  $\varepsilon$  displacement length. This is corrected by *shifting* the mask this length. We also analytically determine the optimum *smoothing* for a hyperbolic

tangent profile. We then describe an efficient numerical approach to calculate optimal smoothing and shifting corrections for *general* masks using a Riccati transformation. We finally examine two analytically solvable problems with additional effects; *Poiseuille flow* (pressure gradients), and *viscous stagnation point flow* (normal and tangential flow, and Re dependent nonlinearities). Stagnation point flow is important as a minimal example of the influence of Re on the emergence of the intermediate and strong damping regimes.

- In section 6 we validate our results experimentally. We briefly outline the efficient spectral code Dedalus, and use it to simulate time-dependent accelerating flow past a rotating 2D cylinder. We generate numerical reference solutions using Dedalus, and again validate our prescriptions. We finally show how Richardson extrapolation can be applied to optimized masks to further boost the numerical convergence to  $\mathcal{O}(\eta^2)$ .
- Finally in section 7 we give a short summary of simple corrections to optimize volume penalty implementations, and corresponding error and cost estimates, and outline future directions.

## 2 Definitions

### 2.1 No-slip boundary conditions

Incompressible fluid dynamics with rigid bodies is normally modelled by partitioning the domain  $\Omega$  into a solid  $\Omega_s$  and fluid  $\Omega_f$  component. On  $\Omega_f$  we solve the viscous incompressible Navier-Stokes equations,

$$\partial_t u + \frac{1}{\rho} \nabla p - \nu \nabla^2 u + u \cdot \nabla u - f = 0, \quad (2)$$

$$\nabla \cdot u = 0, \quad (3)$$

for the fluid velocity  $u$  and the pressure  $p$ , given a kinematic viscosity  $\nu$ , constant density  $\rho$ , and external body force  $f$ . We incorporate the solid by specifying no-slip boundary conditions on  $u$  along the interface  $\partial\Omega_s$ ,

$$u = u_s \quad \text{on} \quad \partial\Omega_s, \quad (4)$$

where  $u_s$  is the velocity of the solid at the boundary.

*Drag and torque calculations* — The core aim of studying fluid-solid interactions is to understand the effect of the fluid on the solid and vice versa. This is commonly quantified by calculating the physically meaningful drag  $F$  and torque  $T$  on the body. These are calculated using the surface stress integrals

$$F_0 = \int_{\partial\Omega_s} \Sigma \cdot \hat{n} dA, \quad \text{and} \quad T_0 = \int_{\partial\Omega_s} r \times (\Sigma \cdot \hat{n}) dA, \quad (5)$$

where  $n$  is the outward pointing unit vector along the solid boundary  $\partial\Omega_s$ , and  $\Sigma$  is the fluid stress

$$\Sigma = -pI + \rho\nu(\nabla u + \nabla u^\top). \quad (6)$$

## 2.2 Volume penalization

The volume penalty method approximates this solution implicitly by replacing no-slip boundary conditions with an added linear damping in the momentum equation,

$$\partial_t u + \frac{1}{\rho} \nabla p - \nu \nabla^2 u + u \cdot \nabla u - f = -\frac{1}{\tau} \Gamma(x, t)(u - u_s), \quad (7)$$

where the *mask function*  $\Gamma : \Omega \rightarrow [0, 1]$  represents the location of the solid (which may evolve in time). The small damping timescale  $\tau$  strongly suppresses the deviation of the fluid and solid velocity where the mask  $\Gamma$  is non-zero<sup>1</sup>. This equation can then be solved on a domain  $\Omega$  that no longer needs to conform to the solid geometry.

The penalty mask  $\Gamma$  is traditionally chosen as [3, 4, 26, 35, 39, 34, 13, 14]

$$\Gamma(x, t) = \begin{cases} 1 & x \in \Omega_s(t), \\ 0 & x \in \Omega_f(t), \end{cases} \quad (8)$$

as shown in fig. 1. The foundational result of this method is that the solution to the above penalized equations (eq. (7) and eq. (8)) converges to the *true* solution (equations eq. (2) to eq. (4)) in the limit  $\tau \rightarrow 0$ , with an  $L^2$  norm of the error in the fluid of order  $\mathcal{O}(\tau^{1/2})$  [10].

However, the mask does not need to coincide with the desired boundary. This paper shows that exploiting additional degrees of freedom in the mask boundary behaviour (such as location and smoothness) can improve convergence to  $\mathcal{O}(\tau)$  in  $L^1$  norm.

This technique also leads to a very simple method for calculating the force on a boundary. Rather than performing the above surface stress integral [6], the force  $F$  and torque  $T$  can be approximated with volume integrals of the penalization term over the full domain [3],

$$F = \rho \int_{\Omega} \frac{\Gamma}{\tau} (u - u_s) dV + \rho \int_{\Omega_s} (\partial_t u_s - f) dV + \int_{\partial\Omega_{in}} \Sigma \cdot \hat{n} dS, \quad (9)$$

$$T = \rho \int_{\Omega} \frac{\Gamma}{\tau} r \times (u - u_s) dV + \rho \int_{\Omega_s} r \times (\partial_t u_s - f) dV + \int_{\partial\Omega_{in}} r \times (\Sigma \cdot \hat{n}) dS. \quad (10)$$

The first correction term is integrated over the desired solid boundary  $\Omega_s$  to account for forcing within the mask  $\Gamma$ . Note that the mask and solid region do *not* necessarily coincide. This term is analogous to the unsteady correction from [13, 37]. The final correction term accounts for the possibility of interior no-slip boundaries  $\partial\Omega_{in}$  within the volume penalized object (as in fig. 1). Both of these corrections are necessary in section 6.

This approach also possesses a physical interpretation. This penalty term corresponds directly to the Darcy drag of the Brinkman equations used to model fluid flow in a porous medium [4]. Decreasing the damping time scale  $\tau$  represents a physical reduction in the permeability of our solid.

## 2.3 Non-dimensionalization

We non-dimensionalize the problem according to characteristic length scale  $L$  and velocity scale  $U$  of the large-scale fluid motion. This could correspond to the size and speed of a rigid object in the fluid flow for example. These induce three important non-dimensional parameters; The *Reynolds number*  $\text{Re}$ , the *damping time scale*  $\eta$ , and the *damping length scale*  $\varepsilon$

$$\text{Re} \equiv \frac{UL}{\nu}, \quad \eta \equiv \frac{\tau U}{L}, \quad \varepsilon \equiv \frac{\sqrt{\nu\tau}}{L}. \quad (11)$$

---

<sup>1</sup>Previous authors [3, 10, 26] have used various symbols for the damping parameter. We use  $\tau$  to signify the dimensional damping timescale. We will use  $\eta$  for the non-dimensionalized time scale.

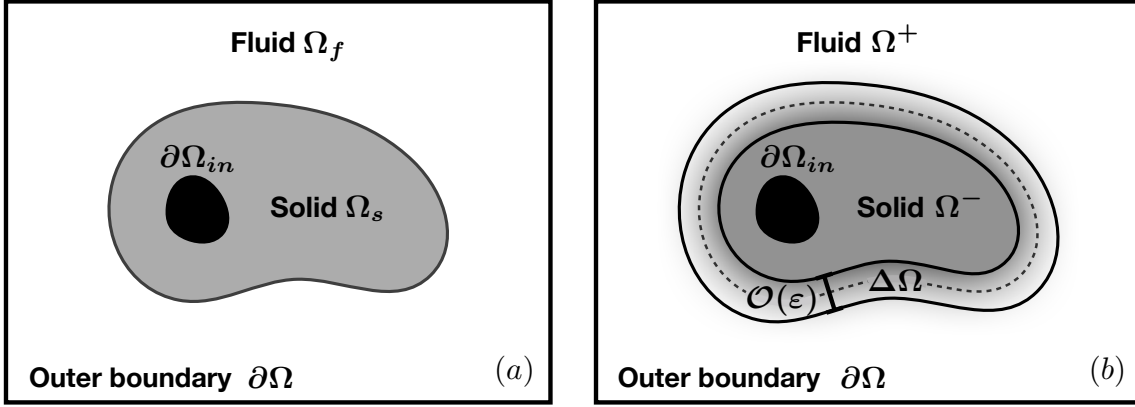


Figure 1: The first figure (a) shows the outer domain boundary  $\partial\Omega$ , the fluid domain  $\Omega_f$ , the volume penalized solid domain  $\Omega_s$  and a possible interior no-slip boundary  $\partial\Omega_{in}$  of the volume penalty method, using traditional co-incident penalization eq. (128). The second figure (b) shows the asymptotic regions considered in section 4 for more general masks. The asymptotic fluid domain  $\Omega^+$  and solid domain  $\Omega^-$  are separated by an  $\mathcal{O}(\varepsilon)$  boundary layer region  $\Delta\Omega$ . The variation of the mask (gray) occurs within the boundary layer  $\Delta\Omega$ .

The Reynolds number  $\text{Re}$  characterizes the ratio of viscous and inertial time scales, the damping *time* scale  $\eta$  measures the separation of damping and inertial time scales, and the damping *length* scale  $\varepsilon$  comes from balancing the viscous and damping terms. Understanding these parameters is key to understanding (and improving) the accuracy of the volume penalty method.

The damping time  $\eta$  and length  $\varepsilon$  are closely related via the Reynolds number  $\text{Re}$

$$\eta = \text{Re} \varepsilon^2, \quad (12)$$

and are equal when  $\eta = \text{Re}^{-1} = \varepsilon$ . Either side of this equality, one of the scales will dominate, leading to multiple damping regimes: *Intermediate damping*  $1 > \eta > \varepsilon > \text{Re}^{-1}$  implies the  $\mathcal{O}(\eta)$  time scale error (from balancing pressure gradients and damping) dominates the  $\mathcal{O}(\varepsilon)$  length scale error (from balancing viscosity and damping). *Strong damping*  $1 > \text{Re}^{-1} > \varepsilon > \eta$  implies the  $\mathcal{O}(\varepsilon)$  length scale error is instead dominant (see fig. 3). This paper will show ways to eliminate both these sources of error.

We then write the penalized equations as

$$\partial_t u + u \cdot \nabla u + \nabla p - \frac{1}{\text{Re}} \nabla^2 u - f = -\frac{1}{\eta} \Gamma(x, t)(u - u_s), \quad (13)$$

where  $u$  and  $p$  are penalized solutions. We denote the solutions to the ‘true’ non-dimensional Navier-Stokes equations, using no-slip boundary conditions on  $\partial\Omega_s$ , by a zero subscript (e.g.  $u_0, p_0$ ), in keeping with the convergence of the penalized solution  $u$  to the true solution  $u_0$  as  $\varepsilon \rightarrow 0$ .

**Remark 2.1** (Error vs computational effort). *The damping induces both a length scale  $\mathcal{O}(\varepsilon)$  and time scale  $\mathcal{O}(\eta) = \mathcal{O}(\text{Re} \varepsilon^2)$  which must be resolved numerically. Therefore the degrees of freedom of the simulation (number of Fourier modes, number of grid points etc) must scale as  $\varepsilon^{-D}$ , where  $D$  is the number of dimensions, and the number of time steps for a given simulation time scales as  $\varepsilon^{-2}$ . Therefore the total effort to perform a simulation scales as  $\varepsilon^{-(D+2)}$ . Given an error scaling of  $\varepsilon^\alpha$ , the total effort required to halve the error is*

$$\text{Effort to halve error} \propto 2^{(D+2)/\alpha}. \quad (14)$$

*For the existing theoretical error scaling of  $\varepsilon^1$ , this implies halving the error requires 16 times the effort in two dimensions, and 32 times the effort in three dimensions. It is thus essential to improve the error scaling  $\alpha$ .*

## 2.4 Error metrics and the displacement length

We first aim to quantify the accuracy of the volume penalty method separate to any numerical discretization error. The three metrics we define measure the flow accuracy in an average and worst-case sense, and the physically meaningful error in the drag calculation.

**Definition 2.1** (Global error  $\mathcal{E}_1$ ). *The  $L^1$  norm of the difference of the penalized solution  $u$  from the reference solution  $u_0$  in the fluid domain,*

$$\mathcal{E}_1 = \|u - u_0\|_{L^1(\Omega_f)} = \frac{1}{|\Omega_f|} \int_{\Omega_f} |u - u_0| dV. \quad (15)$$

**Definition 2.2** (Local error  $\mathcal{E}_\infty$ ). *The  $L^\infty$  norm of the difference of the penalized solution  $u$  from the reference solution  $u_0$  in the fluid domain,*

$$\mathcal{E}_\infty = \|u - u_0\|_{L^\infty(\Omega_f)} = \max_{x \in \Omega_f} |u - u_0|. \quad (16)$$

**Definition 2.3** (Drag error  $\Delta F$ , Torque error  $\Delta T$ ). *The difference between the volume integral for the penalized drag  $F$  (torque  $T$ ) to the surface stress integral for the reference drag  $F_0$  (reference torque  $T_0$ ) on a true no slip boundary.*

$$\Delta F = F - F_0, \quad \Delta T = T - T_0. \quad (17)$$

It is worth elaborating on the choice of fluid error norms  $\mathcal{E}_1$  and  $\mathcal{E}_\infty$ . Strictly,

$$\frac{\mathcal{E}_1}{\mathcal{E}_\infty} \leq \text{support}(u - u_0), \quad (18)$$

where  $\text{support}(u - u_0)$  is the volume of the region on which  $u \neq u_0$ . However, the support is a considerable overestimate of the localization of the error. If  $|u - u_0| \approx \varepsilon$  in a region of size  $d$ , and much smaller elsewhere (though still non-zero), then  $\mathcal{E}_1 \approx \varepsilon d$  (for a unit volume domain), while  $\mathcal{E}_\infty \approx \varepsilon$ . The ratio of these two  $\mathcal{E}_1/\mathcal{E}_\infty \approx d$  captures this approximate localization of the error.

The key insight of this paper is that conventional masks do *not* optimize the global error  $\mathcal{E}_1$  or the drag error  $\Delta F$  with respect to the penalty parameter  $\varepsilon$ . This is because in general the far field behaviour of the penalized velocity  $u$  is shifted by an amount proportional to the boundary layer length scale  $\varepsilon$ , corresponding to a different size solid than the mask function. This difference is what we call the *displacement length*  $\ell^*$  of the volume penalty method, which we now define in words as,

**Definition 2.4** (Displacement length  $\ell^*$ ). *(i). The difference in size between the desired no-slip boundary  $\partial\Omega_s$ , and a hypothetical no-slip boundary  $\partial\Omega_s^*$  the mask function  $\Gamma$  “most closely” approximates. (ii). Alternatively, the difference in size between the desired no-slip boundary  $\partial\Omega_s$ , and the optimal mask function  $\Gamma^*$  that most closely approximates it.*

This definition of the displacement length can refer to the size of the mask or the desired no-slip boundary. We use these meanings interchangeably as they relate to the same phenomenon: the ideal mask is in general not the same shape or size as the solid we wish to approximate.

The concrete advance of this paper is a simple method to offset the displacement length error. We do so by refining the edge of the mask (near the boundary) to localize the error to the boundary layer. This implies restricting the  $\mathcal{O}(\varepsilon)$  error in the (tangential) velocity to an  $\mathcal{O}(\varepsilon)$  region, and achieving  $\mathcal{O}(\varepsilon^2)$  accuracy in the remainder of the fluid, leading to  $\mathcal{E}_1 = \mathcal{O}(\varepsilon^2)$  error. The continued  $\mathcal{O}(\varepsilon)$  local error  $\mathcal{E}_\infty$  illustrates this localization of the error to a small region. We then show that this error localization also improves the physically meaningful drag and torque errors  $\Delta F$  and  $\Delta T$  to  $\mathcal{O}(\varepsilon^2)$ .

## 2.5 Mask functions

We now define normalized mask functions  $\widehat{\Gamma}$ , the and the translations and scaling used to define general masks  $\Gamma$ .

**Definition 2.5** (Normalized mask function  $\widehat{\Gamma}$ ). *A function on  $\mathbb{R}$  which satisfies*

1. *Boundedness:*  $\widehat{\Gamma} : \mathbb{R} \rightarrow [0, 1]$ .
2. *Limiting behaviour:*  $\lim_{x \rightarrow -\infty} \widehat{\Gamma}(x) = 1$  and  $\lim_{x \rightarrow \infty} \widehat{\Gamma}(x) = 0$ .
3. *Monotonicity:*  $x_2 > x_1 \implies \widehat{\Gamma}(x_2) < \widehat{\Gamma}(x_1)$ .
4. *Symmetry:*  $\widehat{\Gamma}(x) + \widehat{\Gamma}(-x) = 1$ .
5. *Normalization:*  $\left. \frac{d\widehat{\Gamma}}{dx} \right|_{x=0} = -1$ .

In this paper we consider smooth normalized mask functions and more restrictive compact normalized mask functions. We note any smooth normalized mask function  $\widehat{\Gamma}$  can be made to interpolate between 0 and 1 in a compact interval  $[-c, c]$  using [5],

$$\widehat{\Gamma}^c(x) = \widehat{\Gamma} \left( \frac{x}{\sqrt{1 - x^2/c^2}} \right) \quad \text{where} \quad -c < x < c. \quad (19)$$

General mask functions  $\Gamma_{\ell, \delta}$  can be generated from a normalized mask function  $\widehat{\Gamma}$  by scaling  $\delta$  and translation  $\ell$ ,

$$\Gamma_{\ell, \delta}(x) = \widehat{\Gamma} \left( \frac{x - \ell}{\delta} \right). \quad (20)$$

We note that discontinuous masks are the limiting case of smooth functions as the thickness approaches zero. In essence, the standard approach is to take the limit  $\delta \rightarrow 0$  first, then consider convergence as  $\varepsilon \rightarrow 0$ . This paper shows that this is not the optimal approach. Namely, choosing a particular  $\ell$  or  $\delta \propto \varepsilon$  cancels the leading order error of the volume penalty method. For concreteness, we consider two example smooth mask functions.

- *Hyperbolic tangent mask*  $\widehat{\Gamma}_{\tanh}$

$$\widehat{\Gamma}_{\tanh}(x) = \frac{1}{2} (1 - \tanh 2x). \quad (21)$$

- *Error function mask*  $\widehat{\Gamma}_{\text{erf}}$

$$\widehat{\Gamma}_{\text{erf}}(x) = \frac{1}{2} (1 - \text{erf} \sqrt{\pi} x). \quad (22)$$

We also consider compactified versions thereof,  $\widehat{K}_{[\tanh; c]}$ ,  $\widehat{K}_{[\text{erf}; c]}$ , which are compact on the interval  $[-c, c]$ .

Finally, we note that these definitions can be extended to higher dimensions by defining a locally conformal coordinate system at the mask boundary and applying the one dimensional mask functions in the wall-normal direction. We now examine the construction of such a coordinate system.

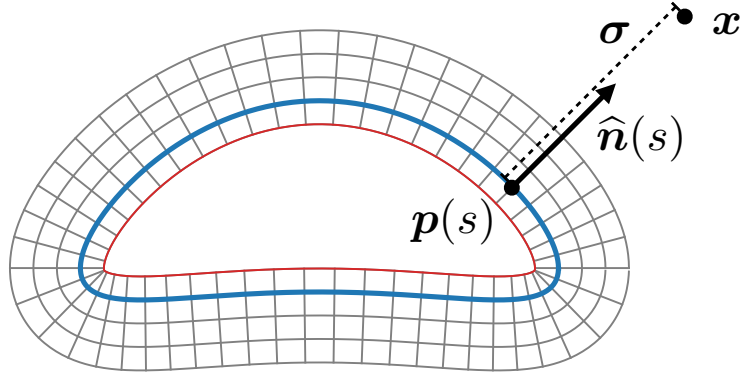


Figure 2: The signed distance function coordinate system. The boundary (blue) is parameterized by surface coordinates  $s$ . A point off the boundary  $x$  can be reached by moving a distance  $\sigma$  in the normal direction  $\hat{n}(s)$  from the closest point on the manifold  $p(s)$ . The surface and normal coordinates are by definition orthogonal, and conform to the boundary. Coordinate singularities (the corners of the red surface) will occur depending on the curvature of the boundary.

### 3 Boundary layer coordinates

In order to understand the error of the volume penalty method, we must analyze the region near the fluid-solid boundary. This requires a choice of coordinate system. A Cartesian system will prove unwieldy for general shapes. A better choice should satisfy two constraints. It should firstly conform to the boundary, so that a single coordinate is used to move off the boundary. It should secondly be everywhere *orthogonal*, to simplify the vector calculus. Infinitely many choices can be made, but a particularly simple choice comes from mapping each point in space to its closest point on the boundary, which is a lower dimensional (smooth) manifold. Specifically, near the boundary, we can parameterize the Cartesian coordinates  $x$  as

$$x = p(s) + \sigma \hat{n}(p(s)), \quad (23)$$

where  $p(s)$  is the closest point on the boundary  $\partial\Omega_s$ , labelled by orthogonal boundary coordinates  $s$ ,  $\hat{n}(s)$  is the normal unit vector at  $p(s)$ , and  $\sigma$  is the *signed distance function*, as illustrated in fig. 2.

This new curvilinear coordinate system will affect all the vector calculus operations when expressed in coordinates, and we develop these expressions in stages. Given the coordinate transform, we can immediately write the inverse Jacobian,

$$\frac{\partial}{\partial \sigma} = \hat{n} \cdot \nabla, \quad \frac{\partial}{\partial s_i} = \frac{\partial p}{\partial s_i} \cdot (I + \sigma \nabla \hat{n}) \cdot \nabla. \quad (24)$$

The normal derivative is straightforward, but the tangential derivatives contain scaling factors. To understand them, we first analyze calculus on the manifold, then probe the normal on the manifold, and finally determine the scaling factor off the manifold.

#### 3.1 Surface vector calculus

On the manifold, we first specify coordinates  $s = (s_1, s_2)$ , which map to points  $p(s)$  in Cartesian space. If we specify that these coordinates are also orthogonal, they induce a tangent vector

basis, a unit vector basis, and a cotangent vector basis which are all parallel,

$$t_i = \frac{\partial p}{\partial s_i}, \quad \hat{t}_i = \frac{t_i}{|t_i|}, \quad \nabla_{s_i} = \frac{\hat{t}_i}{|t_i|}. \quad (25)$$

We can then write the surface gradient  $\nabla_{\perp}$  as

$$\nabla_{\perp} = \nabla_{s_1} \frac{\partial}{\partial s_1} + \nabla_{s_2} \frac{\partial}{\partial s_2} = \frac{\hat{t}_1}{|t_1|} \frac{\partial}{\partial s_1} + \frac{\hat{t}_2}{|t_2|} \frac{\partial}{\partial s_2} = \hat{t}_1 \nabla_1 + \hat{t}_2 \nabla_2. \quad (26)$$

Given knowledge of the surface area measure from the scale factors we can then determine the surface divergence as the adjoint of the gradient,

$$dA = |t_1||t_2| ds_1 ds_2 \implies \nabla_{\perp} \cdot u_{\perp} = \frac{1}{|t_1||t_2|} \left( \frac{\partial}{\partial s_1} (|t_2|u_1) + \frac{\partial}{\partial s_2} (|t_1|u_2) \right). \quad (27)$$

### 3.2 Surface normal

We then consider the normal to the manifold, calculated with the cross product

$$\hat{t}_1 \times \hat{t}_2 = \hat{n}. \quad (28)$$

It is not difficult to use the definition of the coordinate transform to show the normal is also the gradient of the signed distance function

$$\hat{n} = \nabla \sigma. \quad (29)$$

This implies that the normal is its own dual vector, and is the key reason for the utility of the signed distance function coordinate system.

Hence, the gradient of the normal is the Hessian of the signed distance function, which is a necessarily symmetric 2-tensor. Hence  $\nabla \hat{n}$  can be diagonalized using its eigenbasis. Since the unit normal is also a unit vector, we conclude that it is a zero eigenvector of  $\nabla \hat{n}$ ,

$$\hat{n} \cdot \hat{n} = 1 \text{ and } \nabla \hat{n} = \nabla \nabla \sigma \implies (\nabla \hat{n}) \cdot \hat{n} = \hat{n} \cdot \nabla \hat{n} = 0 \quad (30)$$

We also know that the remaining eigenvectors must be orthogonal to  $\hat{n}$ , and so lie within the tangent space to the manifold. Without loss of generality, we can let the surface coordinates lie parallel to these eigenvectors. These directions are the principal directions of curvature, and their eigenvalues correspond to the (negative) of the principal curvature of the surface in that direction

$$\nabla \hat{n} = -\kappa_1 \hat{t}_1 \hat{t}_1 - \kappa_2 \hat{t}_2 \hat{t}_2 = -K, \quad (31)$$

where  $K$  is the surface curvature tensor, or the shape operator.

### 3.3 Vector calculus in the boundary region

To move off the manifold, we note that the basis vectors are independent of  $\sigma$ . This gives us a basis for the velocity vectors

$$u = u_{\sigma} \hat{n} + u_{\perp}, \quad \text{where } u_{\perp} = u_1 \hat{t}_1 + u_2 \hat{t}_2. \quad (32)$$

Note that the tangential velocity is in the tangent space to the manifold for  $\sigma = 0$ . We can then invert the previous relation to calculate the gradient off the manifold

$$\nabla = \hat{n} \partial_{\sigma} + J^{-1} \cdot \nabla_{\perp}, \quad \text{where } J = I - \sigma K. \quad (33)$$

We note that the determinant of  $J$  is

$$|J| = 1 - \sigma \bar{K} + \sigma^2 |K|, \quad \text{where } \bar{K} = \kappa_1 + \kappa_2, \text{ and } |K| = \kappa_1 \kappa_2. \quad (34)$$

The trace  $\bar{K}$  and determinant  $|K|$  of the shape operator are the mean curvature and Gaussian curvature respectively. This gives us the full volume measure

$$dV = |J| d\sigma dA = |J| |t_1| |t_2| d\sigma ds_1 ds_2, \quad (35)$$

which can be used to calculate the volume divergence (as the adjoint of the gradient)

$$\nabla \cdot u = \frac{\partial_\sigma(|J|u_\sigma)}{|J|} + \frac{\nabla_\perp \cdot (\hat{J}u_\perp)}{|J|}, \quad (36)$$

where we have defined for convenience the adjugate matrices

$$\hat{J} = |J|J^{-1} = I - \sigma \hat{K} \quad \hat{K} = |K|K^{-1} = \kappa_2 \hat{t}_1 \hat{t}_1 + \kappa_1 \hat{t}_2 \hat{t}_2, \quad (37)$$

which have the effect of swapping the principal curvatures in the shape operator. Note that the Jacobian and related operators only ever operate on the tangent vectors, so we can think of them as  $2 \times 2$  matrices. The scalar Laplacian is simply calculated as the divergence of a scalar gradient

$$\nabla^2 f = \frac{\partial_\sigma(|J|\partial_\sigma f)}{|J|} + \frac{\nabla_\perp \cdot (\hat{J}J^{-1}\nabla_\perp f)}{|J|}. \quad (38)$$

We can then define the curl as the unique operator (up to sign) which satisfies  $\nabla \cdot \nabla \times = \nabla \times \nabla = 0$ ,

$$\nabla \times u = -\hat{n} \frac{\nabla_\perp \cdot (\hat{J}u^\perp)}{|J|} + \hat{J}^{-1}(\partial_\sigma(\hat{J}u^\perp) - \nabla^\perp u_\sigma), \quad (39)$$

where for convenience we have define rotated quantities as

$$\nabla^\perp = \hat{n} \times \nabla_\perp, \quad u^\perp = \hat{n} \times u_\perp, \quad (40)$$

which satisfy the useful identities

$$\nabla^\perp \cdot \nabla_\perp = \nabla_\perp \cdot \nabla^\perp = 0, \quad u^\perp \cdot u_\perp = u_\perp \cdot u^\perp = 0, \quad (41)$$

$$\hat{n} \times (Ju_\perp) = \hat{J}u^\perp, \quad \hat{n} \times u^\perp = -u_\perp. \quad (42)$$

We can then calculate the vector Laplacian using curl, divergence, and gradient as

$$\begin{aligned} \nabla^2 u = \hat{n} \left[ \partial_\sigma \left( \frac{\partial_\sigma(|J|u_\sigma) + \nabla_\perp \cdot (\hat{J}u_\perp)}{|J|} \right) - \frac{\nabla_\perp \cdot (\hat{J}J^{-1}(\partial_\sigma(Ju_\perp) - \nabla_\perp u_\sigma))}{|J|} \right] \\ + \hat{J}^{-1} \partial_\sigma \left( \hat{J}J^{-1}(\partial_\sigma(Ju_\perp) - \nabla_\perp u_\sigma) \right) + J^{-1} \nabla_\perp \left( \frac{\partial_\sigma(|J|u_\sigma)}{|J|} \right) + \Delta_\perp u_\perp, \end{aligned} \quad (43)$$

where

$$\Delta_\perp u_\perp = J^{-1} \nabla_\perp \left( \frac{\nabla_\perp \cdot (\hat{J}u_\perp)}{|J|} \right) + \hat{J}^{-1} \nabla^\perp \left( \frac{\nabla^\perp \cdot (Ju_\perp)}{|J|} \right). \quad (44)$$

The divergence-free vector Laplacian of incompressible hydrodynamics simplifies to

$$-\nabla \times \nabla u = \frac{\hat{n}}{|J|} \left[ -\nabla_{\perp} \cdot (\hat{J}J^{-1}(\partial_{\sigma}(Ju_{\perp}) - \nabla_{\perp}u_{\sigma})) \right] \quad (45)$$

$$+ \hat{J}^{-1}\partial_{\sigma} \left( \hat{J}J^{-1}(\partial_{\sigma}(Ju_{\perp}) - \nabla_{\perp}u_{\sigma}) \right) + \hat{J}^{-1}\nabla^{\perp} \left( \frac{\nabla^{\perp} \cdot (Ju_{\perp})}{|J|} \right).$$

The key generalization is to calculate the vector gradients. Orthonormal basis vectors imply antisymmetric relations

$$\hat{n} \cdot \hat{t}_i = 0 \implies \nabla \hat{n} \cdot \hat{t}_i = -\nabla \hat{t}_i \cdot \hat{n}, \quad (46)$$

$$\hat{t}_i \cdot \hat{t}_j = 0 \implies \nabla \hat{t}_i \cdot \hat{t}_j = -\nabla \hat{t}_j \cdot \hat{t}_i, \quad (47)$$

We also know the normal derivative for all tangent vectors is zero, hence the gradient is simply a scaled version of the surface gradient of each vector

$$\partial_{\sigma}\hat{n} = \partial_{\sigma}\hat{t}_i = 0 \implies \nabla \hat{n} = J^{-1} \cdot \nabla_{\perp}\hat{n}, \quad \nabla \hat{t}_i = J^{-1} \cdot \nabla_{\perp}\hat{t}_i, \quad (48)$$

and the surface gradients are constrained to be

$$\nabla_{\perp}\hat{n} = -\kappa_1\hat{t}_1\hat{t}_1 - \kappa_2\hat{t}_2\hat{t}_2 \quad \nabla_{\perp}\hat{t}_i = \kappa_i\hat{t}_i\hat{n} + \mathcal{R}_i^{jk}\hat{t}_j\hat{t}_k, \quad (49)$$

where the (intrinsic) Ricci rotation coefficients are antisymmetric  $\mathcal{R}_i^{jk} = -\mathcal{R}_k^{ji}$ , and have only two free nonzero components

$$\mathcal{R}_1^{12} = \hat{t}_1 \cdot (\nabla \hat{t}_1) \cdot \hat{t}_2 = \omega_1, \quad \mathcal{R}_2^{21} = \hat{t}_2 \cdot (\nabla \hat{t}_2) \cdot \hat{t}_1 = -\omega_2. \quad (50)$$

We then calculate the vector gradient using the Ricci rotation coefficients

$$\nabla u = \hat{n}\hat{n}\partial_{\sigma}u_{\sigma} + \hat{n}\partial_{\sigma}u_{\perp} + J^{-1}(\nabla_{\perp}u_{\sigma} + Ku_{\perp})\hat{n} + J^{-1}(\nabla_{\perp}u_{\perp} - Ku_{\sigma}). \quad (51)$$

This allows us to give the convective derivative as

$$u \cdot \nabla u = \hat{n} \left( u_{\sigma}\partial_{\sigma}u_{\sigma} + u_{\perp} \cdot J^{-1}(\nabla_{\perp}u_{\sigma} + Ku_{\perp}) \right) \quad (52)$$

$$+ u_{\sigma}\partial_{\sigma}u_{\perp} + u_{\perp} \cdot J^{-1}(\nabla_{\perp}u_{\perp} - Ku_{\sigma}).$$

These give us all the vector calculus operators required to rewrite the Navier-Stokes equations, and higher order tensorial calculus in general.

## 4 Asymptotic expansions

We now analyze volume penalization for an object of arbitrary (smooth) shape, in a fluid with general forcing. Our analysis uses a body-centred frame, so this general forcing will include acceleration terms, as well as other possibilities. To do so, we first split the problem into three areas – the fluid region outside the object  $\Omega^+$ , the solid region inside the object  $\Omega^-$ , and the thin boundary region between these two domains  $\Delta\Omega$  as in fig. 1 (b). These regions are distinguished by the behaviour of the mask function  $\Gamma$ , which is zero, one, and varying in the fluid, solid and boundary regions respectively. The signed distance function coordinate system allows a convenient analysis of the boundary region. We then apply an asymptotic expansion in  $\varepsilon$  to each of these problems, along with a rescaling of the normal coordinate by  $\varepsilon$  for the boundary region. To solve the problem order by order, we apply asymptotic matching conditions as  $\varepsilon \rightarrow 0$  in intermediate zones between adjacent regions. The leading order problem gives a

simple justification of the convergence of the volume penalty method to the ideal solution. The first order problem demonstrates general  $\mathcal{O}(\varepsilon)$  displacement length error for the volume penalty method. However, a simple correction to the boundary can offset the displacement length and achieve  $\mathcal{O}(\varepsilon^2)$  accuracy in velocity and pressure in the fluid. We defer constructive examples of these corrections to section 5. The second order problem demonstrates the emergence of two asymptotic error regimes: *intermediate damping*  $1 > \eta > \text{Re}^{-1}$  for which the error is dominated by  $\eta$ , and *strong damping*  $\eta < \text{Re}^{-1}$  for which the error is dominated by  $\varepsilon$ , as in fig. 3. We finally show how the improved flow accuracy extends to the both the force and torque calculations defined earlier.

## 4.1 Fluid problem

In the fluid region  $\Omega^+$  we have  $\Gamma = 0$  (with at most exponentially small error), and write the velocity and pressure in the fluid as  $u^+$  and  $p^+$ . This gives the system,

$$\nabla \cdot u^+ = 0, \quad (53)$$

$$\frac{\partial u^+}{\partial t} - \frac{1}{\text{Re}} \nabla^2 u^+ + \nabla p^+ + u^+ \cdot \nabla u^+ = f, \quad (54)$$

$$u^+ = U \quad \text{on} \quad \partial\Omega, \quad (55)$$

We then expand the velocity and pressure in the fluid as an asymptotic series:

$$u^+ \sim \sum_{k=0} \varepsilon^k u_k^+, \quad p^+ \sim \sum_{k=0} \varepsilon^k p_k^+ \quad \text{as} \quad \varepsilon \rightarrow 0. \quad (56)$$

This sum is in practice truncated at some point, depending on the desired order of expansions. We will only examine up to second order expansions. By assuming  $\varepsilon$  is asymptotically small, we conclude each order of  $\varepsilon$  must individually satisfy each equation. This implies all expansions are divergence free

$$\nabla \cdot u_k^+ = 0, \quad k = 0, 1, \dots, \quad (57)$$

and all higher order expansions satisfy homogeneous boundary conditions

$$u_0^+ = U \quad \text{on} \quad \partial\Omega, \quad \text{and} \quad u_k^+ = 0 \quad \text{on} \quad \partial\Omega, \quad k = 1, 2, \dots \quad (58)$$

The momentum equations become

$$\frac{\partial u_0^+}{\partial t} - \frac{1}{\text{Re}} \nabla^2 u_0^+ + \nabla p_0^+ + u_0^+ \cdot \nabla u_0^+ - f = 0, \quad (59)$$

$$\frac{\partial u_1^+}{\partial t} - \frac{1}{\text{Re}} \nabla^2 u_1^+ + \nabla p_1^+ + u_0^+ \cdot \nabla u_1^+ + u_1^+ \cdot \nabla u_0^+ = 0, \quad (60)$$

$$\frac{\partial u_2^+}{\partial t} - \frac{1}{\text{Re}} \nabla^2 u_2^+ + \nabla p_2^+ + u_0^+ \cdot \nabla u_2^+ + u_2^+ \cdot \nabla u_0^+ = -u_1^+ \cdot \nabla u_1^+, \quad (61)$$

and so on for higher orders.

## 4.2 Solid problem

In the solid we have  $\Gamma = 1$  (again with only exponentially small error). We denote velocity and pressure as  $u^-$  and  $p^-$ , and write our equations as,

$$\nabla \cdot u^- = 0, \quad (62)$$

$$\frac{\partial u^-}{\partial t} - \frac{1}{\text{Re}} \nabla^2 u^- + \frac{1}{\text{Re} \varepsilon^2} u^- + \nabla p^- + u^- \cdot \nabla u^- = f. \quad (63)$$

We similarly expand the velocity and pressure in the solid as an asymptotic series:

$$u^- \sim \sum_{k=0} \varepsilon^k u_k^-, \quad p^- \sim \sum_{k=0} \varepsilon^k p_k^- \quad \text{as } \varepsilon \rightarrow 0. \quad (64)$$

and derive divergence-free conditions

$$\nabla \cdot u_k^- = 0, \quad k = 0, 1, \dots \quad (65)$$

Using these constraints in the momentum equations it is possible to then derive

$$\nabla^2 p_0^- = \nabla \cdot f, \quad u_0^- = 0, \quad (66)$$

$$\nabla^2 p_1^- = 0, \quad u_1^- = 0, \quad (67)$$

$$\nabla^2 p_2^- = 0, \quad u_2^- = \text{Re}(f - \nabla p_0^-). \quad (68)$$

Higher order expansions behave analogously.

### 4.3 Boundary layer problem

The boundary layer  $\Delta\Omega$  exists in an  $\mathcal{O}(\varepsilon)$  region around the true boundary  $\partial\Omega_s$  which divides the fluid and solid regions (fig. 1 (b)). The  $\mathcal{O}(\varepsilon)$  size of the boundary domain is motivated by the damping length scale induced by the penalty-viscous balance; As this length scale must be resolved, we will assume the mask function is at most smoothness  $\delta = \mathcal{O}(\varepsilon)$  as  $\varepsilon \rightarrow 0$ . Excess smoothness  $\delta \gg \varepsilon$  would introduce added error to the problem (as the mask intrudes into the fluid), and waste excess resolution on resolving the mask. In this region the mask function varies between the extremal values and is kept fully in the momentum equations,

$$\nabla \cdot u = 0, \quad (69)$$

$$\frac{\partial u}{\partial t} - \frac{1}{\text{Re}} \nabla^2 u + \frac{1}{\text{Re} \varepsilon^2} \Gamma u + \nabla p + u \cdot \nabla u = f. \quad (70)$$

As we focus on a boundary layer of size  $\mathcal{O}(\varepsilon)$  around the boundary, we adopt the rescaled normal coordinate  $\xi$ ,

$$\sigma \rightarrow \varepsilon \xi \quad \implies \quad \partial_\sigma \rightarrow \frac{1}{\varepsilon} \partial_\xi \quad (71)$$

This implies asymptotic expansions of the scaling factors

$$J \rightarrow 1 - \varepsilon \xi K \quad |J| \rightarrow 1 - \varepsilon \xi \bar{K} + \varepsilon^2 \xi^2 |K| \quad (72)$$

$$J^{-1} \rightarrow \sum_{k=0}^{\infty} \varepsilon^k \xi^k K^k \quad |J|^{-1} \rightarrow \sum_{k=0}^{\infty} \varepsilon^k \xi^k \left( \sum_{l=0}^k \kappa_1^l \kappa_2^{k-l} \right) \quad (73)$$

We then expand each operator in an asymptotic series. The gradient becomes

$$\nabla = \varepsilon^{-1} \hat{n} \partial_\xi + \sum_{k=0}^{\infty} \varepsilon^k \xi^k K^k \nabla_\perp. \quad (74)$$

The divergence can be written as

$$|J| \nabla \cdot u = \varepsilon^{-1} \partial_\xi u_\sigma - \partial_\xi (\xi \bar{K} u_\sigma) + \nabla_\perp \cdot u_\perp + \varepsilon \left( \partial_\xi (\xi^2 |K| u_\sigma) - \xi \nabla_\perp \cdot (\hat{K} u_\perp) \right), \quad (75)$$

The convective derivative becomes

$$u \cdot \nabla u = \varepsilon^{-1} (u_\sigma \partial_\xi u_\perp + \hat{n} u_\sigma \partial_\xi u_\sigma) + \sum_{k=0}^{\infty} \varepsilon^k \xi^k u_\perp K^k \cdot ((\nabla_\perp u_\perp - K u_\sigma) + (\nabla_\perp u_\sigma + K u_\perp) \hat{n}) \quad (76)$$

The most complicated is the (divergence free) vector Laplacian.

$$\nabla^2 u = \varepsilon^{-2} \partial_\xi^2 u_\perp + \varepsilon^{-1} (-\bar{K} \partial_\xi u_\perp - \partial_\xi \nabla_\perp u_\sigma - \hat{n} \nabla_\perp \cdot (\partial_\xi u_\perp)) + \mathcal{O}(1) \quad (77)$$

We then also expand the variables as an asymptotic series

$$u \sim \sum_{k=0} \varepsilon^k (u_{\sigma k} \hat{n} + u_{\perp k}) \quad p \sim \sum_{k=0} \varepsilon^k p_k \quad \text{as } \varepsilon \rightarrow 0. \quad (78)$$

#### 4.4 Matching conditions

After deriving each order problem for each region, we must solve them by applying matching boundary conditions. We do this by enforcing asymptotic agreement between adjacent regions in an intermediate buffer zone  $\xi \sim \varepsilon^{-1/2}$  – asymptotically large for the inner problem, but without coordinate singularities (provided  $\varepsilon \ll \min_i |\kappa_i^{-1}|$ ), and asymptotically small for the outer problem. This means

$$\lim_{\varepsilon \rightarrow 0} u(\pm \varepsilon^{-1/2} \xi, s, t) \sim \lim_{\varepsilon \rightarrow 0} u^\pm(\pm \varepsilon^{+1/2} \xi, s, t). \quad (79)$$

Each variable is composed of asymptotic expansions, so we match order by order in  $\varepsilon$ . However each outer expansion of the fluid or solid variables can be further expanded with Taylor expansions about the true boundary at  $\partial\Omega_s$ . Put together this simplifies the matching conditions to

$$\lim_{\xi \rightarrow \pm\infty} u(\xi) = \sum_{k=0} \varepsilon^k u_k \sim \sum_{k=0} \varepsilon^k \left( \sum_{j=0}^k \frac{\xi^j}{j!} \partial_\sigma^j u_{k-j}^\pm(0^\pm) \right). \quad (80)$$

#### 4.5 Zeroth order problem and the tangential boundary layer

We now write the leading order problem for the fluid, solid, and boundary regions, and solve them using matching conditions. We will see that the leading order solution is equivalent to the true solution of the Navier-Stokes equations, justifying the use of the volume penalty method.

*Fluid problem* — As shown, the fluid problem is

$$\nabla \cdot u_0^+ = 0, \quad (81)$$

$$\frac{\partial u_0^+}{\partial t} - \frac{1}{\text{Re}} \nabla^2 u_0^+ + \nabla p_0^+ + u_0^+ \cdot \nabla u_0^+ = f, \quad (82)$$

$$u_0^+ = 0 \quad \text{on } \partial\Omega. \quad (83)$$

*Solid problem* — The leading order solid problem is

$$\nabla^2 p_0^- = \nabla \cdot f, \quad u_0^- = 0. \quad (84)$$

*Boundary problem* — The leading order boundary problem illustrates the structure of the subsequent orders. The divergence condition reduces to purely the normal direction, and implies

the normal velocity is constant. Matching to the solid problem requires this to be zero, giving a no-flux boundary condition for the fluid velocity,

$$\partial_\xi u_{\sigma 0} = 0 \quad \Longrightarrow \quad u_{\sigma 0} = 0 \quad \Longrightarrow \quad u_{\sigma 0}^+(0) = 0. \quad (85)$$

**Tangential velocity boundary layer** — We now analyze the tangential velocities with the leading order momentum equation, which takes the form

$$(\Gamma - \partial_\xi^2)u_{\perp 0} = 0. \quad (86)$$

We emphasize the importance of this leading order operator, as it appears with the highest order term in every subsequent order problem, and is key to understanding the behaviour of the volume penalty method. Noting the asymptotic behaviour of the mask function (zero or one), we can infer the asymptotic behaviour of the kernel. The first unphysical solution  $\mathcal{V}$  is normalized to tend to one as  $\xi \rightarrow +\infty$ , and grows exponentially as  $\xi \rightarrow -\infty$ , so will not occur in our expansions,

$$\mathcal{V}(\xi \rightarrow -\infty) \sim ae^{-\xi} \quad \mathcal{V}(\xi \rightarrow +\infty) \sim 1. \quad (87)$$

The *physical* solution  $\mathcal{U}$  instead decays exponentially as  $\xi \rightarrow -\infty$ , and is normalized to have unit gradient as  $\xi \rightarrow +\infty$ ,

$$\mathcal{U}(\xi \rightarrow -\infty) \sim be^\xi \quad \mathcal{U}(\xi \rightarrow +\infty) \sim \xi - \ell^*. \quad (88)$$

This shift  $\ell^*$  is key to understanding the volume penalty method, and represents the *displacement length* of the mask. Example physical solutions for different choices of  $\Gamma$  are shown in section 5, fig. 4.

The solid matching condition tells us that  $u_{\perp 0}$  is some multiple of the  $\mathcal{U}$  solution.

$$u_{\perp 0} = A_{\perp 0}\mathcal{U} \quad (89)$$

However the fluid matching condition instead requires asymptoting to a constant in the fluid. The only solution with zero gradient in both limits is the zero solution, implying no-slip boundary conditions at  $\partial\Omega_s$  for the fluid velocities,

$$u_{\perp 0}(\xi \rightarrow \infty) \sim u_{\perp 0}^+(0) \quad \Longrightarrow \quad u_{\perp 0} = A_{\perp 0} = u_0^+(0) = 0. \quad (90)$$

This tells us that the leading order problem is equivalent to the incompressible Navier-Stokes equations with no-slip boundaries at  $\sigma = 0$ , validating the convergence of the volume penalty method. We now continue with the next order problem, the leading order error, and show how it can be controlled through judicious choice of  $\Gamma$ .

## 4.6 First order problem and displacement length error

*Fluid problem* — In the fluid we now have

$$\nabla \cdot u_1^+ = 0, \quad (91)$$

$$\frac{\partial u_1^+}{\partial t} - \frac{1}{\text{Re}} \nabla^2 u_1^+ + \nabla p_1^+ + u_0^+ \cdot \nabla u_1^+ + u_1^+ \cdot \nabla u_0^+ = 0, \quad (92)$$

$$u_1^+ = 0 \quad \text{on} \quad \partial\Omega. \quad (93)$$

*Solid problem* — The solid then gives

$$\nabla^2 p_1^- = 0, \quad u_1^- = 0. \quad (94)$$

*Boundary problem* — The continuity equation for the boundary problem implies the first order normal velocity is again constant, which is zero by matching with the solid boundary condition

$$\partial_\xi u_{\sigma 1} - \bar{K} \partial_\xi (\xi u_{\sigma 0}) + \nabla_\perp \cdot u_{\perp 0} = \partial_\xi u_{\sigma 1} = 0 \quad \Longrightarrow \quad u_{\sigma 1} = 0. \quad (95)$$

Hence the normal velocity is at most  $\mathcal{O}(\varepsilon^2)$  around the boundary. The normal component of the momentum equation simplifies to imply that the leading order behaviour of the pressure is constant

$$\frac{1}{\text{Re}} (\Gamma u_{\sigma 1} + \nabla_\perp \cdot (\partial_\xi u_{\perp 0})) + \partial_\xi p_0 + u_{\sigma 0} \partial_\xi u_{\sigma 0} = \partial_\xi p_0 = 0 \quad \Longrightarrow \quad p_0 = p_0^\pm(0). \quad (96)$$

**Error bounds for general masks** — The tangential ( $\perp$ ) component of the momentum equation simplifies to

$$(\Gamma - \partial_\xi^2) u_{\perp 1} + \bar{K} \partial_\xi u_{\perp 0} + \partial_\xi \nabla_\perp u_{\sigma 0} + \text{Re} u_{\sigma 0} \partial_\xi u_{\perp 0} = (\Gamma - \partial_\xi^2) u_{\perp 1} = 0, \quad (97)$$

Matching to the solid problem implies  $u_{\perp 1}$  is some multiple of  $\mathcal{U}$

$$u_{\perp 1} = A_{\perp 1} \mathcal{U}, \quad (98)$$

and matching the fluid problem gives us the boundary condition for  $u_{\perp 1}^+$ ,

$$\begin{aligned} A_{\perp 1} \mathcal{U} \sim u_{\perp 1}^+(0) + \xi \partial_\sigma u_{\perp 0}^+(0) & \Longrightarrow & A_{\perp 1} &= \partial_\sigma u_{\perp 0}^+(0), \\ & \Longrightarrow & u_{\perp 1}^+(0) &= -\partial_\sigma u_{\perp 0}^+(0) \ell^*. \end{aligned} \quad (99)$$

This shift  $\ell^*$  corresponds to the  $x$ -intercept of the asymptotic fluid solution  $u_1^+$  — this is the *displacement length* of the mask. Importantly it depends only on the choice of mask  $\Gamma$ . Most masks  $\ell^*$  give displacement length  $\ell^*$  order unity (see section 5 for examples), implying the boundary condition  $u_{\perp 1}^+(0) = \mathcal{O}(\varepsilon)$ , which in turn implies the leading order error will be  $\mathcal{O}(\varepsilon)$  throughout the fluid.

**Error bounds for optimal masks** — However, if we choose a mask with zero displacement length ( $\ell^* = 0$ ), we obtain homogenous boundary conditions in the fluid,

$$u_1^+|_{\sigma=0} = 0 \quad \text{on} \quad \partial\Omega_s, \quad \text{and} \quad u_1^+ = 0 \quad \text{on} \quad \partial\Omega. \quad (100)$$

If the errors  $u_1^+$  and  $p_1^+$  are initially zero, the homogeneous linear momentum equation implies they will remain so for all time. In reality, any small perturbation will grow over time (according to the Lyapunov time scale of the flow), but this is inherent to the chaotic nature of most fluid-flows, and not a limitation of this specific method. The statistical behaviour of the fluid will be accurate to  $\mathcal{O}(\varepsilon^2)$  with this correction. We show how to choose a mask with no displacement error in section 5, but first analyze the second order problem, and in doing so find the emergence of two Re dependent asymptotic regimes.

## 4.7 Second order equation and different volume penalty regimes

*Fluid problem* — The problem in the fluid region is as for the previous order with added convection terms,

$$\nabla \cdot u_2^+ = 0, \quad (101)$$

$$\frac{\partial u_2^+}{\partial t} - \frac{1}{\text{Re}} \nabla^2 u_2^+ + \nabla p_2^+ + u_0^+ \cdot \nabla u_2^+ + u_2^+ \cdot \nabla u_0^+ = -u_1^+ \cdot \nabla u_1^+, \quad (102)$$

$$u_2^+ = 0 \quad \text{on} \quad \partial\Omega. \quad (103)$$

For an optimal mask  $u_1^+$  is zero, giving a homogeneous linear equation in the fluid.

*The solid problem* — The important difference of the second order problem is that the flow in the solid is non-zero, and forced entirely by the leading order pressure and forcing within the solid,

$$\nabla^2 p_2^- = 0, \quad u_2^- = \text{Re}(f - \nabla p_0^-). \quad (104)$$

*The boundary problem* — The incompressibility equation simplifies since  $u_{\sigma 1} = 0$ ,

$$\partial_\xi u_{\sigma 2} - \bar{K} \partial_\xi (\xi u_{\sigma 1}) + \nabla_\perp \cdot u_{\perp 1} = \partial_\xi u_{\sigma 2} + \nabla_\perp \cdot u_{\perp 1} = 0. \quad (105)$$

Using the solution for the first order problem, we find  $u_{\sigma 2}$  is,

$$u_{\sigma 2} = u_{\sigma 2}(-\infty) - \nabla_\perp \cdot (\partial_\sigma u_0^+(0)) \int_{-\infty}^\xi \mathcal{U} d\zeta. \quad (106)$$

We can simplify noting that at the boundary  $\sigma = 0^\pm$ ,

$$u_{\sigma 2}(-\infty) = \text{Re}(f_\sigma - \partial_\sigma p_0^-)_{\sigma=0^-}, \quad \nabla_\perp \cdot (\partial_\sigma u_0^+(0)) = \text{Re}(f_\sigma - \partial_\sigma p_0^+)_{\sigma=0^+}, \quad (107)$$

where the first equality comes from matching to the solid solution, and the second equality comes from evaluating the normal component of the fluid momentum equation at the solid boundary  $\partial\Omega_s$  ( $\sigma = 0$ ). This behaves asymptotically as a constant plus an exponential within the solid, and quadratically within the fluid,

$$\text{as } \xi \rightarrow -\infty \quad u_{\sigma 2} \sim \text{Re} \left[ (f_\sigma(0^-) - \partial_\sigma p_0^-(0)) (1 - be^\xi) \right], \quad (108)$$

$$\text{as } \xi \rightarrow +\infty \quad u_{\sigma 2} \sim \text{Re} \left[ (f_\sigma(0^+) - \partial_\sigma p_0^+(0)) \frac{\xi^2}{2} + A_{\sigma 2} \xi + B_{\sigma 2} \right]. \quad (109)$$

The quadratic behaviour is consistent with the leading order problem, and the linear behaviour matches onto zero for an optimized mask ( $A_{\sigma 2} \propto \ell$ ). However, the constant behaviour into the fluid depends on the jump in the pressure derivative (and external forcing) across the boundary, which depends on the details of the flow, and cannot be eliminated using a passive mask, so in general  $B_{\sigma 2}$  is non-zero. Hence, the boundary condition for normal velocity in the fluid scales with the *Reynolds number*  $\text{Re}$ .

We can also derive an equation for the pressure by taking the divergence of the momentum equation in the boundary region to obtain

$$\partial_\xi^2 p_1 = \bar{K} \partial_\xi p_0 - \frac{1}{\text{Re}} \partial_\xi \Gamma u_{\sigma 2} + \partial_\xi f_\sigma, \quad (110)$$

at first order. Integration of this equation shows the discontinuity in the normal pressure gradient across the mask boundary.

We can then determine the tangential velocity using the tangential momentum equation,

$$(\Gamma - \partial_\xi^2) u_{\perp 2} = -\bar{K} \partial_\xi u_{\perp 1} + \text{Re}(f_\perp - \nabla_\perp p_0). \quad (111)$$

This is solved using variation of parameters,

$$u_{\perp 2} = \mathcal{Q} \mathcal{U}, \quad (112)$$

$$\text{where } \mathcal{Q} = \int \frac{-\mathcal{R} \mathcal{W} \mathcal{U}^{-1} d\xi + c}{\mathcal{W}} \quad \text{and} \quad \mathcal{W} = \exp \left( \int \frac{2\mathcal{U}'}{\mathcal{U}} d\xi \right), \quad (113)$$

where  $\mathcal{R}$  is the right hand side of eq. (111) and  $c$  is a constant of integration.

**Reynolds dependent error regimes** — These equations show that the boundary condition for the second order error in the fluid scales with the Reynolds number  $\text{Re}$ . This means the second order error is proportional to  $\eta$ , while the first order error is proportional to  $\varepsilon$ . If  $\text{Re}$  is sufficiently large  $\text{Re} > \varepsilon^{-1}$ , then the asymptotic separation of the first and second order corrections is no longer valid, and the “second order” *time* scale error of size  $\mathcal{O}(\text{Re} \varepsilon^2) = \mathcal{O}(\eta)$  dominates the “first order” *length* scale error  $\mathcal{O}(\varepsilon)$ .

This means volume penalization leads to multiple asymptotic damping regimes, depending on the relative size of the damping time scale  $\eta$ , and the damping length scale  $\varepsilon$ , illustrated in fig. 3. If  $\eta > 1$  (the region on the left of the graph), the fluid is damped too slowly, and remains  $\mathcal{O}(1)$  within the solid, meaning the error is  $\mathcal{O}(1)$ . If  $\varepsilon > 1$  (the region below the top left-bottom right diagonal in the plane), the damping is insufficient to overcome the viscosity of the fluid, leading to  $\mathcal{O}(1)$  velocity within the solid, and hence  $\mathcal{O}(1)$  error. Note that this regime can occur even for large  $\eta$ , provided the Reynolds number is sufficiently small  $1 \gg \eta > \text{Re}$ .

Ignoring these computationally useless regimes of large error, there are two remaining regimes. The *intermediate* damping regime (light gray) occurs when the Reynolds number is large enough to promote the second order system to dominance, when  $1 > \eta > \varepsilon > \text{Re}^{-1}$ . This regime gives the appearance of  $\mathcal{O}(\varepsilon^2)$  convergence even for unoptimized masks, but this is only temporary, as seen in [4].

Once the damping is sufficiently large ( $1 > \text{Re}^{-1} > \varepsilon > \eta$ ) the damping length scale  $\varepsilon$  always dominates the time scale  $\eta$ . This is the *strong* damping regime (white), for which it is necessary to apply mask corrections to promote the convergence to  $\mathcal{O}(\varepsilon^2)$ .

**Reynolds dependent cost regimes** — We can further analyze the computational cost regimes for large  $\text{Re}$  by comparing the damping length scale  $\varepsilon$  and time scale  $\eta$  with the intrinsic Kolmogorov length scale  $\lambda$  and CFL time scale  $t$  in three dimensional turbulence. After non-dimensionalizing according to the outer velocity scale  $U$ , outer length scale  $L$ , kinematic viscosity  $\nu$  and damping time scale  $\tau$ , we can express the non-dimensional parameters in terms of  $\eta$  and  $\text{Re}$ .

$$\text{Re} = \frac{UL}{\nu}, \quad \eta = \frac{\tau U}{L}, \quad \varepsilon = \sqrt{\frac{\eta}{\text{Re}}}, \quad t = \text{Re}^{-3/4}, \quad \lambda = \text{Re}^{-3/4}. \quad (114)$$

We need the numerical grid resolution  $\Delta x$  and time step size  $\Delta t$  to resolve the smallest of each time and length scale,

$$\Delta x = \min(\varepsilon, \lambda) \quad \text{and} \quad \Delta t = \min(\eta, t). \quad (115)$$

Given the computational cost  $C$  is proportional to the degrees of freedom  $\Delta x^{-3} \Delta t^{-1}$ , and a scaling for the damping in terms of the Reynolds number  $\eta = \text{Re}^{-\alpha}$ , we find several damping regimes for  $\text{Re} \ll 1$ ,

$$\alpha < 1/2 \quad \implies \quad \lambda = t < \varepsilon < \eta \quad \implies \quad C \sim \lambda^{-3} t^{-1} = \text{Re}^3 \quad (116)$$

$$1/2 < \alpha < 3/4 \quad \implies \quad \varepsilon < \lambda = t < \eta \quad \implies \quad C \sim \varepsilon^{-3} t^{-1} = \eta^{-3/2} \text{Re}^{3/4} \quad (117)$$

$$3/4 < \alpha < 1 \quad \implies \quad \varepsilon < \eta < \lambda = t \quad \implies \quad C \sim \varepsilon^{-3} \eta^{-1} = \eta^{-5/2} \text{Re}^{3/2} \quad (118)$$

$$1 < \alpha \quad \implies \quad \eta < \varepsilon < \lambda = t. \quad (119)$$

This implies that arbitrarily shaped boundaries using volume penalization can be added to turbulent simulations for no extra cost at an error of  $\text{Re}^{-1/2}$ . Beyond this regime  $\alpha > 1/2$ , the computational cost scales more aggressively in  $\eta$ . This has given the impression that low  $\text{Re}$  simulations are more difficult using volume penalization. However, this also implies it is easier to reach the terminal strong damping regime  $\alpha > 1$ , beyond which mask corrections of the displacement length can eliminate the leading order error and regain  $\mathcal{O}(\varepsilon^2)$  convergence. We therefore extend the practicability of the volume penalty method to low  $\text{Re}$ .

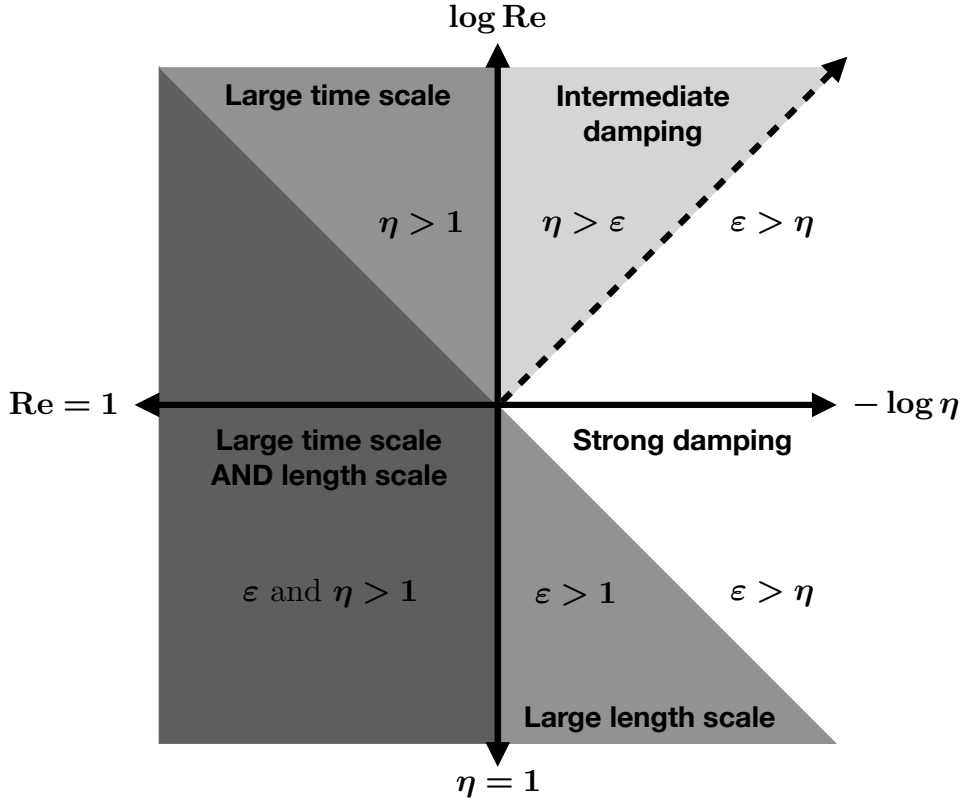


Figure 3: Different volume penalty regimes plotted logarithmically as a function of the Reynolds number  $\text{Re}$  (vertical axis) and damping time scale  $\eta$  (horizontal axis). The regions are distinguished by the relative size of the damping length scale  $\varepsilon$  and damping time scale  $\eta$ . Increased damping (smaller  $\eta$ ) corresponds to moving right on the diagram. The two darkest regions are where at least one of  $\eta$  or  $\varepsilon$  are greater than 1, and the solution is completely incorrect. Our correction is useful in the strong damping regime (white), which is the limiting regime as  $\eta \rightarrow 0$  for any fixed  $\text{Re}$ . For  $\text{Re} > 1$ , an intermediate regime arises (light gray), in which the damping time scale dominates the damping length scale  $1 > \eta > \varepsilon > \text{Re}^{-1}$ .

## 4.8 Force calculation

We now relate the integral of the penalty term to the force and torque calculations. For a general mask, the integral of the penalty term can be rewritten using the penalized Navier-Stokes equations

$$\int_{\Omega} \frac{1}{\text{Re} \varepsilon^2} \Gamma u \, dV = \int_{\Omega} \nabla \cdot \Sigma - \frac{Du}{Dt} + f \, dV. \quad (120)$$

where the non-dimensional fluid stress is

$$\Sigma = -pI + \frac{1}{\text{Re}} (\nabla u + \nabla u^{\top}). \quad (121)$$

Note that we use a body-centered coordinate frame and account for the acceleration terms in the body forcing  $f$ . For a mask with compact support  $\Omega^+$ , which is  $\mathcal{O}(\varepsilon)$  larger than  $\Omega_s$ , we can restrict this integral to this region (with exponentially small error for decaying masks such as  $\Gamma_{\tanh}$ )

$$\int_{\Omega} \frac{1}{\text{Re} \varepsilon^2} \Gamma u \, dV = \int_{\Omega^+} \nabla \cdot \Sigma - \frac{Du}{Dt} + f \, dV. \quad (122)$$

The divergence theorem relates this to the stress along  $\partial\Omega^+$ , plus corrections

$$\int_{\Omega} \frac{1}{\text{Re } \varepsilon^2} \Gamma u \, dV = \int_{\partial\Omega^+} \Sigma \cdot \hat{n} \, dS - \int_{\partial\Omega_{in}} \Sigma \cdot \hat{n} \, dS + \int_{\Omega^+} -\frac{Du}{Dt} + f \, dV. \quad (123)$$

We can compare the penalized stress  $\Sigma$  with the true stress  $\Sigma_0$

$$\int_{\Omega} \frac{1}{\text{Re } \varepsilon^2} \Gamma u \, dV = \int_{\partial\Omega^+} (\Sigma_0 + \Sigma - \Sigma_0) \cdot \hat{n} \, dS - \int_{\partial\Omega_{in}} \Sigma \cdot \hat{n} \, dS + \int_{\Omega^+} -\frac{Du}{Dt} + f \, dV. \quad (124)$$

We can then relate the true stress on the mask support boundary  $\partial\Omega^+$  to the true stress on the true boundary  $\partial\Omega_s$  by Stokes' theorem with the unpenalized equation for  $u_0, p_0$

$$\int_{\partial\Omega_s} \Sigma_0 \cdot \hat{n} \, dS = \int_{\Omega} \frac{1}{\text{Re } \varepsilon^2} \Gamma u \, dV + \int_{\partial\Omega_{in}} \Sigma \cdot \hat{n} \, dS - \int_{\Omega_s} f \, dV \quad (125)$$

$$- \int_{\partial\Omega^+} (\Sigma - \Sigma_0) \cdot \hat{n} \, dS \quad (126)$$

$$- \int_{\Omega^+ - \Omega_s} \frac{Du_0}{Dt} \, dV + \int_{\Omega^+} \frac{Du}{Dt} \, dV. \quad (127)$$

The penalized stress on no-slip boundaries interior to the mask (such as in section 6) and the  $f$  volume integral are both order unity in general, so must be subtracted off (note that  $f$  is integrated over exactly  $\Omega_s$ ). The leading stress error  $\Sigma - \Sigma_0$  is  $\mathcal{O}(\varepsilon)$  at  $\Omega^+$  for general masks, as both  $p_1^+$  and  $u_1^+$  are non-zero in the fluid, implying  $\mathcal{O}(\varepsilon)$  convergence of the force calculation.

However, an optimal mask ensures that  $p_1^+$  and  $u_1^+$ , and hence  $\Sigma - \Sigma_0$  are accurate to  $\mathcal{O}(\varepsilon^2)$  at the mask boundary  $\partial\Omega^+$ , so this term is now  $\mathcal{O}(\varepsilon^2)$  accurate. The remaining acceleration terms are  $\mathcal{O}(\varepsilon^2)$  in general. This is because both  $u_0$  and  $\varepsilon u_1$  are at most  $\mathcal{O}(\varepsilon)$  in the region  $\Omega^+ - \Omega_s$ , which only has support  $\mathcal{O}(\varepsilon)$ . The  $\mathcal{O}(\varepsilon)$  error  $u_1$  decays exponentially fast into the solid, so also has support and magnitude of  $\mathcal{O}(\varepsilon)$ , integrating to  $\mathcal{O}(\varepsilon^2)$ . The  $\mathcal{O}(\varepsilon^2)$  error  $u_2^-$  and  $p_2^-$  have support throughout the solid region, but again integrate to only  $\mathcal{O}(\varepsilon^2)$ . Hence, by choosing an optimal mask, the dominant stress error can be eliminated and the force calculation accuracy promoted to  $\mathcal{O}(\varepsilon^2)$ .

## 4.9 Torque calculations

The torque calculation proceeds similarly. We recover the correct stress at  $\partial\Omega^+$  to  $\mathcal{O}(\varepsilon^2)$ , and we need to show this is only  $\mathcal{O}(\varepsilon^2)$  different from the true stress at  $\partial\Omega_s$ . It does not immediately seem that the divergence theorem can be used because  $r \times (\nabla \cdot \Sigma_0)$  is not a divergence. However it does hold. It relies on the fact that the stress tensor is symmetric, and that the gradient of the coordinate vector is the identity tensor. Then, following the same procedure as for the force calculation, one finds  $\mathcal{O}(\varepsilon)$  accuracy for the torque for general masks, and  $\mathcal{O}(\varepsilon^2)$  accuracy for optimal masks.

## 5 Choosing optimal masks

We now show how to construct optimal masks for the inner problem of section 4 eq. (86). We first consider the traditional mask, with a discontinuity at the intended solid boundary. This can easily be solved analytically, and reveals a non-zero displacement length. This can be corrected by shifting the mask opposite the displacement length. However, the mask can also be smooth, and infinitely many choices are possible. We first consider a solvable example of the tanh function, common in phase-field modelling. We then derive an efficient calculation for

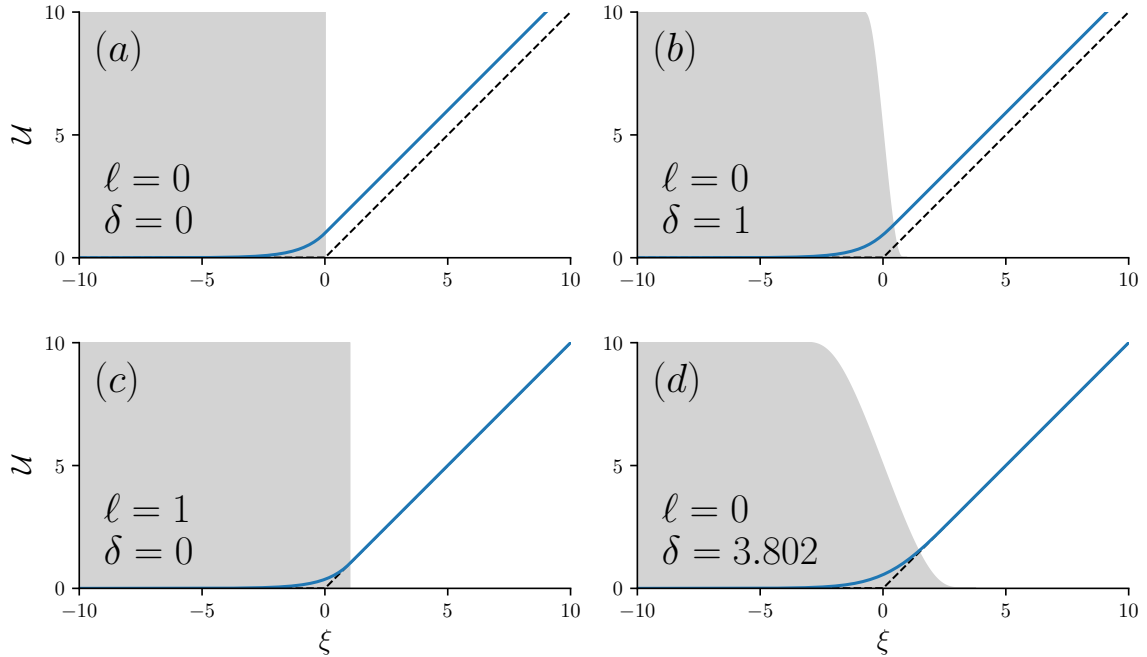


Figure 4: Different mask choices (gray) give different velocity profiles (blue) compared to the ideal solution (dashed black) in the boundary layer problem eq. (86). Figure (a) shows the conventional discontinuous mask, with zero smoothing or shifting, results in a displacement length  $\ell^* = -1$ . Plot (b) shows an unoptimized tanh profile using smoothness  $\delta = 1$  gives  $\mathcal{O}(1)$  displacement length. Plot (c) optimally shifts the standard mask by  $\ell = 1$  to eliminate the displacement length error. Plot (d) shows optimal smoothing  $\delta^*$  (table 1) can also eliminate the displacement length error.

optimal rescalings for general mask functions using a Riccati transform. We finally examine two analytically solvable problems including non-zero pressure gradients (Poiseuille flow), and normal flow and nonlinearity (viscous flow past a stagnation point). The stagnation flow example is particularly important as a minimal example of the Re dependence of different error regimes.

## 5.1 Conventional volume penalization

The conventional form of volume penalization uses a discontinuous step function, centred at  $\xi = 0$ ,

$$\Gamma_{0,0}(\xi) = \begin{cases} 1 & \xi < 0 \\ 0 & \xi > 0 \end{cases}. \quad (128)$$

Enforcing continuity and differentiability at  $\xi = 0$ , we solve to find

$$\mathcal{U}(\xi) = \begin{cases} e^\xi & \xi < 0, \\ 1 + \xi & \xi > 0. \end{cases} \quad (129)$$

The solution has a non-zero displacement length  $\ell^* = -1$ , which implies an  $\mathcal{O}(\varepsilon)$  error in the solution in general. The mask is  $\varepsilon$  “too small”, and must be shifted to offset this error. This is the cause of  $\mathcal{O}(\varepsilon)$  convergence for the traditional volume penalty method. We now need some way to change the mask to eliminate this displacement.

## 5.2 Shifting the mask

The most apparent correction is to simply shift the mask a length  $\ell = 1$  into the fluid (fig. 4 (a) vs fig. 4 (b)). By enforcing  $\mathcal{U} = \xi$  for  $\xi > \ell$ , we see the optimum mask (and shift) are given by

$$\Gamma_{\ell^*,0}(x) = \begin{cases} 1 & \xi < 1, \\ 0 & \xi > 1, \end{cases} \quad \text{so} \quad \ell = 1, \quad (130)$$

giving a penalized velocity  $u$  of

$$\mathcal{U}(\xi) = \begin{cases} e^{\xi-1} & \xi < 1, \\ \xi & \xi > 1. \end{cases} \quad (131)$$

This simple refinement eliminates the displacement error. Section 4 implies that this improves the accuracy of the flow variables  $u^+$ ,  $p^+$  and drag and torque calculations  $\Delta F$  and  $\Delta T$  to  $\mathcal{O}(\varepsilon^2)$ .

## 5.3 Smoothing the mask

The mask does not need to be discontinuous however. We can use a smooth mask function. While this may at first seem inherently less accurate, we show this is not the case. Smoothness in fact *improves* the numerical convergence of almost all methods when the problem is discretized. By carefully calibrating the smoothness, it is possible to again eliminate the displacement length. We first consider a tanh type profile,

$$\Gamma(\xi) = \frac{1}{2} \left( 1 - \tanh \left( \frac{2\xi}{\delta} \right) \right). \quad (132)$$

We define transformed coordinates and variables, and a rescaled smoothness

$$z(\xi) \equiv \frac{1 + \tanh \left( \frac{2\xi}{\delta} \right)}{2}, \quad \mathcal{U}(\xi) = U(z(\xi)), \quad \delta \rightarrow 4n, \quad (133)$$

for which the problem becomes

$$(1 - z)z^2U''(z) + (1 - 2z)zU'(z) - n^2U(z) = 0. \quad (134)$$

The solution which satisfies  $U(0) = 0$  can be written as a Frobenius series

$$U(z) = \frac{1}{2} \sum_{k=0}^{\infty} \frac{\Gamma(k+n)\Gamma(k+n+1)}{\Gamma(k+2n+1)} \frac{z^{k+n}}{k!} = z^n \frac{\Gamma(n)\Gamma(n+1)}{2\Gamma(2n+1)} {}_2F_1(n, n+1, 2n+1, z), \quad (135)$$

where here  $\Gamma$  represents the actual  $\Gamma$  function, and  ${}_2F_1$  is the hypergeometric function. Considering the behaviour of the function as  $z \rightarrow 1$  from below, and applying the transformation, we can show that

$$\mathcal{U}(\xi) \sim z - \sigma(n)\delta, \quad \text{as} \quad \xi \rightarrow \infty, \quad \text{where} \quad \sigma(n) = \frac{1}{2n} + \psi(n) + \gamma \quad (136)$$

where  $\gamma$  is the Euler–Mascheroni constant and  $\psi(n)$  is the digamma function

$$\psi(n) = \frac{\Gamma'(n)}{\Gamma(n)} = -\gamma + \sum_{k=0}^{\infty} \frac{n-1}{(k+n)(k+1)}. \quad (137)$$

We can calculate the value of  $n$  (and hence  $\delta$ ) for which the constant offset is zero

$$\sigma(n) = 0, \quad \text{for} \quad n \approx 0.662057 \quad \text{or} \quad \delta \approx 2.648228. \quad (138)$$

This is the optimal smoothness for a tanh profile which also eliminates the displacement length without requiring an additional shift in the mask.

## 5.4 General corrections via Riccati transform

The previous sections show that there are two simple optimizations available for any mask. We can both *shift* or *smooth* the mask boundary to offset the displacement length. But we must do this numerically for a general mask function. In its current form, this would require solving a second order boundary value form. We now apply a Riccati transform to drastically reduce the cost of solving optimal parameters for a given mask function.

Any mask function  $\Gamma(\xi)$  can be written as a shifted  $\ell$  and scaled  $\delta$  version of a normalized mask function  $\Gamma(\xi) = \widehat{\Gamma}((\xi - \ell)/\delta)$ . We define a scaled coordinate  $z$

$$z = \frac{\xi - \ell}{\delta} \quad (139)$$

Using a Riccati transformation

$$R(z) = \frac{\dot{u}(z)}{u(z)} = \frac{\delta u'(\xi)}{u(\xi)} \quad (140)$$

the first order tangential momentum equation becomes

$$R'(z) + R^2(z) = \delta^2 \widehat{\Gamma}(z) \quad (141)$$

For a mask compact on the interval  $\xi \in [(\ell - c\delta), (\ell + c\delta)]$  ( $z \in [-c, c]$ ), we recover an exponential solution  $u(\xi) \propto e^\xi$  for  $z < -c$ . Differentiating, this gives the initial condition for the Riccati equation

$$R(z = -c) = \delta \frac{u'(\xi)}{u(\xi)} = \delta. \quad (142)$$

We can then use the known linear profile at  $z = c$  to determine the ideal shift  $\ell^*$  in terms of smoothing  $\delta$ . For an ideal shift, the velocity profile is proportional to  $u(z) = z$ . Thus, at  $z = c$ , we have

$$R(z = c) = \frac{\delta}{\ell^* + c\delta} \quad (143)$$

This can be rearranged to give the optimal scaled shift as

$$\ell^*(\delta) = \left( \frac{1}{R(c)} - c \right) \delta \quad (144)$$

This can easily be extended to the noncompact smooth functions by choosing  $c$  according to cutoff of machine error  $10^{-16}$ . This is the (negative) displacement length for a given mask profile.

This transformed system is much easier to solve than the original second order boundary value problem. We solve it numerically using simple Runge-Kutta integrators of the `scipy` python library.

To illustrate this dependence we plot the optimum (scaled) shift  $\ell^*$  as a function of smoothing  $\delta$  for the four representative smooth masks in fig. 5. The limit  $\delta \rightarrow 0$  reproduces the optimum discontinuous shift  $\ell^* = 1$  for all mask types, and as the smoothing increases, the optimum shift decreases.

An important case is the ‘zero-shift’ optimum mask, for which no shifting is necessary to offset the displacement length. These are visible as the intercepts in fig. 5, and are given numerically in table 1. This choice is numerically motivated as it balances requirements of resolving the mask and the velocity field. Moving away from the optimum line, the mask is either too ‘large’ ( $\ell > \ell^*(\delta)$ ), or too small ( $\ell < \ell^*(\delta)$ ).

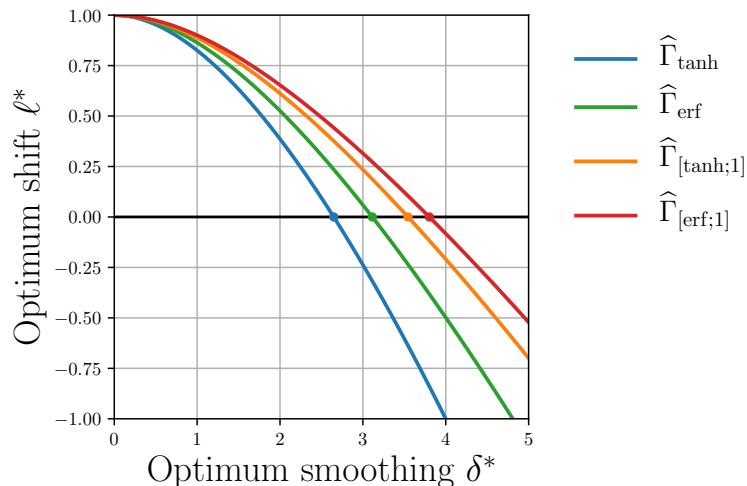


Figure 5: We plot the optimum shift  $\ell^*$  as a function of smoothing  $\delta^*$  for four families of mask function. The limit  $\delta \rightarrow 0$  reproduces the optimum discontinuous shift  $\ell^* = 1$ , and the zero shift smoothing occurs at the intercept of the curves, and are given in table 1.

Table 1: Table of optimal zero-shift smoothing proportionality constants  $\delta^*$  for different normalized mask profiles  $\hat{\Gamma}$ .

| Profile $\hat{\Gamma}$           | Zero-shift optimum smoothing ratio $\delta^*$ |
|----------------------------------|---|
| $\hat{\Gamma}_{\text{erf}}$      | 3.113467865158625                             |
| $\hat{\Gamma}_{[\text{erf};1]}$  | 3.801719284432660                             |
| $\hat{\Gamma}_{\text{tanh}}$     | 2.648228280104068                             |
| $\hat{\Gamma}_{[\text{tanh};1]}$ | 3.544030484658485                             |

## 5.5 Poiseuille flow

Planar Poiseuille flow considers steady flow between two stationary walls driven by a constant pressure gradient. The problem reduces to a single equation for the tangential velocity  $v$  in terms of the wall-normal direction  $x$ ,

$$v'' - \frac{1}{\varepsilon^2}\Gamma(x)v = -2 \quad v'(x \rightarrow -\infty) \rightarrow 0 \quad v(1) = 0, \quad (145)$$

A true no-slip wall is modelled by replacing the damping terms with no-slip boundary conditions at  $x = 0$ . In the fluid, the flow behaves parabolically, and there is an  $\mathcal{O}(\varepsilon^2)$  flow due to pressure within the solid fig. 6. However, the same leading order  $\mathcal{O}(\varepsilon)$  displacement length occurs for each mask – the leading order boundary layer behaviour is identical to the inner problem. Applying the optimized masks of section 5 eliminates the dominant  $\mathcal{O}(\varepsilon)$  displacement length error, but an  $\mathcal{O}(\varepsilon^2)$  contribution remains due to the pressure driven flow (fig. 6 (c)). This problem shows that pressure gradients lead to second order errors. However it lacks interesting geometries, equation nonlinearities, or unsteady behaviour, which all lead to important effects.

## 5.6 Viscous stagnation point flow

Flow about a stagnation point adds two important physical effects to the previous planar problems; flow normal and tangent to a boundary, and equation nonlinearities parameterised by the Reynolds number  $Re$ .

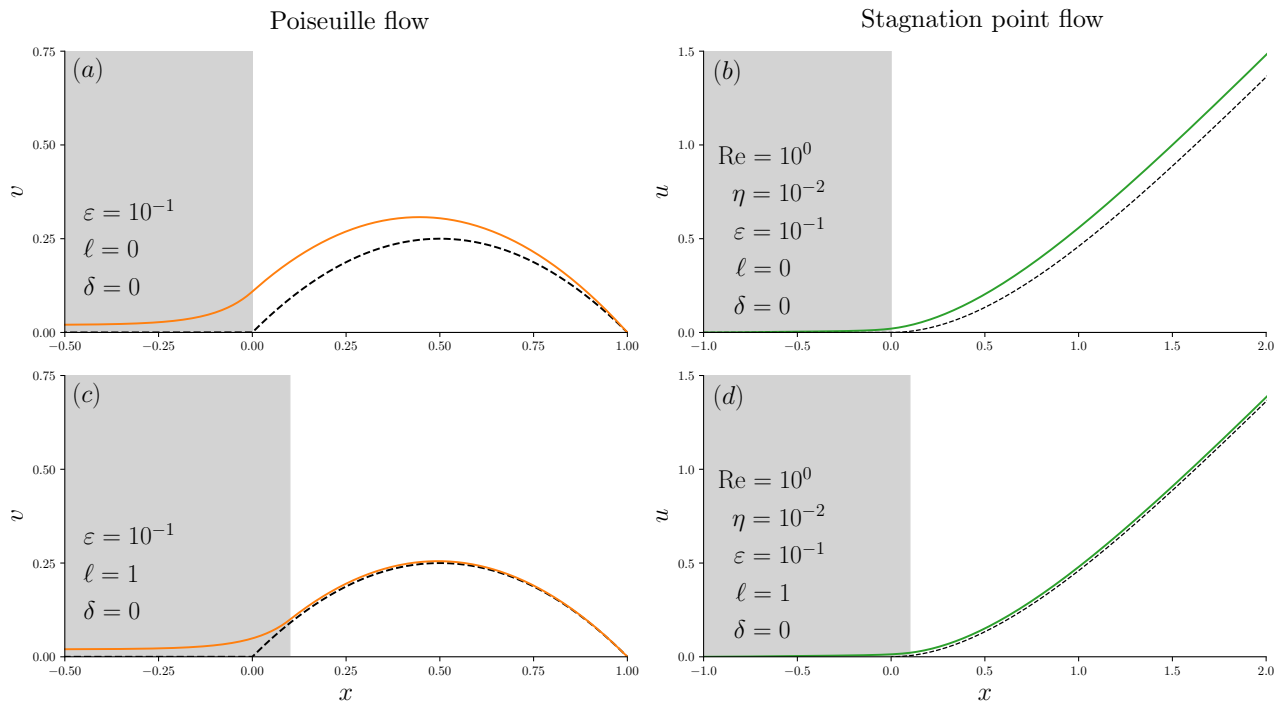


Figure 6: Figure (a) plots the wall-tangential velocity  $v$  (orange) of Poiseuille flow between a true no-slip boundary (at  $x = 1$ ), and a infinite volume penalized boundary beyond  $x < 0$ , for damping length  $\varepsilon = 10^{-1}$ . Figure (b) plots the wall-normal velocity  $u$  (green) of viscous stagnation point flow near a finite volume penalized boundary for  $-1 < x < 0$  at  $\text{Re} = 1$ ,  $\eta = 10^{-2}$ , which gives damping length  $\varepsilon = 10^{-1} > \eta$ , corresponding to strong damping. Both plots use the standard unoptimized discontinuous mask  $\ell = \delta = 0$  and give  $\mathcal{O}(\varepsilon)$  displacement error with respect to the ideal solutions (dashed black). Figure (c) and (d) apply zero-displacement length masks to improve the error to  $\mathcal{O}(\varepsilon^2)$  in the fluid.

We can use symmetry to reduce the two dimensional problem to a single third order nonlinear differential equation for the wall-normal velocity  $u$  in the wall-normal co-ordinate  $x$ . Adding a finite volume penalization boundary, we now solve for the penalized normal velocity  $u$ ,

$$u'^2 - u''u + \frac{1}{\text{Re}}u''' - \frac{\Gamma}{\eta}u' = 1, \quad u(-1) = 0, \quad u'(-1) = 0, \quad u'(\infty) = 1. \quad (146)$$

We cannot extend our volume penalized region indefinitely, due to the linear pressure driven flow in this region, which causes the velocity at  $x = 0$  to increase as the true boundary is moved further away. We instead enforce no slip boundary conditions on  $u$  and  $u'$  at the non-dimensional location  $x = -1$ . To compare with the true profile, we replace the damping term with no-slip conditions applied at  $x = 0$ . We solve the system numerically using Dedalus section 6 [1].

This simple system reproduces the distinction between normal and tangential velocity errors noted in section 4. Specifically, the combination of zero velocity at the boundary and the incompressibility constraint implies zero gradient in the normal velocity at the boundary – the normal velocity is parabolic near the boundary fig. 6 (b), (d). Hence the normal velocity is always  $\mathcal{O}(\varepsilon^2)$  in the boundary region, whereas the tangential velocity can be  $\mathcal{O}(\varepsilon)$ .

Stagnation point flow is also important because it introduces the Reynolds number  $\text{Re}$  in a maximally simple way. It shows how this additional parameter leads to the emergence of an additional damping regime. As in section 4, we witness the transition from intermediate damping (dominant time scale error  $\eta > \varepsilon$ ) to strong damping (dominant length scale error  $\varepsilon > \eta$ ) past  $\eta < \text{Re}^{-1}$  using a plot of the global error  $\mathcal{E}_1$  of  $U$  as a function of  $\eta$ , for different

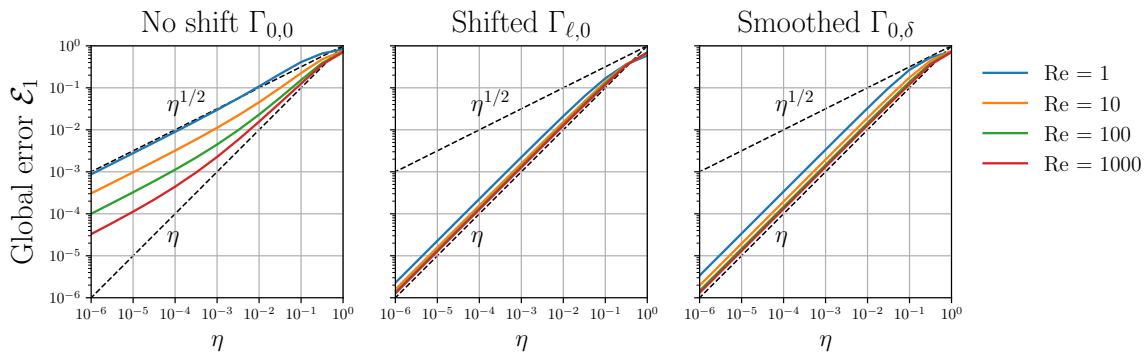


Figure 7: Log-log plots of global error  $\mathcal{E}_1$  as a function of  $\eta = \text{Re} \varepsilon^2$ , for different choices of  $\text{Re} = 1, 10, 10^2, 10^3$  in volume penalized stagnation point flow. Three choices of mask function are shown, being unshifted discontinuous mask  $\Gamma_{0,0}$ , optimum shifted discontinuous mask  $\Gamma_{\varepsilon,0}$ , and optimum smoothed mask  $\Gamma_{0,\delta}$  for the compact error function mask. A clear transition between intermediate and strong damping occurs for the unshifted discontinuous mask. The local error behaves similarly for stagnation point flow.

choices of  $\text{Re}$  in fig. 7. For a general mask, this will restrict the convergence to  $\mathcal{O}(\varepsilon)$  for strong damping. However, a mask with zero displacement length will achieve  $\mathcal{O}(\varepsilon^2)$  convergence even in asymptotically large damping regimes (fig. 6 (d)). In this way, we suggest that the volume penalty method can always achieve  $\mathcal{O}(\varepsilon^2)$  convergence, regardless of  $\text{Re}$ . This peculiar, if fortunate, high Reynolds number behaviour was also observed experimentally by Angot et al. [4], contradicting the theoretical convergence predicted by Angot [3] ( $\mathcal{O}(\varepsilon^{1/2})$ ) and Carbou and Fabrie [10] ( $\mathcal{O}(\varepsilon)$ ).

## 6 Unsteady 2D Flow Past a Rotating Cylinder

We now examine a realistic flow configuration incorporating a broad range of fluid-dynamic phenomena: 2D incompressible flow past a rotating cylinder at moderate Reynolds number. This system includes damping, viscosity, non-linearity, curvilinear geometries, and unsteady linear and rotational acceleration of the flow and body respectively, leading to non-zero unsteady horizontal drag  $F_x$ , vertical drag  $F_y$ , and torque  $T$ . We simulate both a true no-slip cylinder and various volume penalized approximations using the open-source spectral PDE solver Dedalus to determine the local and global error of each field as well as the physically relevant drag and torque accuracy. We compare the performance of standard unoptimized masks with optimally shifted and optimally smoothed masks, validate our prescriptions, and apply a simple Richardson extrapolation scheme to further accelerate the convergence of optimized masks to  $\mathcal{O}(\varepsilon^4) = \mathcal{O}(\eta^2)$  accuracy. The configurations are tested with geometry conforming spectral elements at  $\text{Re} = 200$ , to examine the mathematical convergence in isolation of numerical error. First we examine the mathematical problem.

### 6.1 Mathematical problem

We simulate the volume penalized cylinder of unit radius on an annular domain  $(\theta, r) \in [0, 2\pi] \times [R_1, R_2]$ . We do not include the center to avert the coordinate singularity. We then solve the

initial value problem with zero initial conditions, and governing equations

$$\frac{\partial(ru)}{\partial r} + \frac{\partial v}{\partial \theta} = 0, \quad (147)$$

$$q - \frac{\partial(rv)}{\partial r} + \frac{\partial u}{\partial \theta} = 0, \quad (148)$$

$$r^2 \frac{\partial u}{\partial t} + \frac{1}{\text{Re}} \frac{\partial q}{\partial \theta} + r^2 \frac{\partial p}{\partial r} = +rvq - \frac{1}{\eta} r^2 \Gamma(r)u, \quad (149)$$

$$r^2 \frac{\partial v}{\partial t} - \frac{1}{\text{Re}} \left( r \frac{\partial q}{\partial r} - q \right) + r \frac{\partial p}{\partial \theta} = -ruq - \frac{1}{\eta} r^2 \Gamma(r)(v - r\Omega(t)). \quad (150)$$

This is a slight reformulation of standard incompressible hydrodynamics in polar coordinates. We solve for the radial and polar velocity  $u$  and  $v$ , and have introduced the variables  $p$  and  $q$  to write the problem in first order form (as required for Dedalus), which are related to the true pressure  $P$  and vorticity  $\omega_z$  by

$$p = P + \frac{1}{2}(u^2 + v^2), \quad q = r\omega_z. \quad (151)$$

We also multiply out factors of  $r^{-1}$  to improve the convergence of spectral discretisations of the equations. The outer boundary at  $r = R_2$  applies uniform flow boundary conditions accelerating from rest

$$u(R_2) = g(t) \cos \theta, \quad v(R_2) = -g(t) \sin \theta, \quad \text{where } g(t) = \Gamma_{[\text{erf};1]} \left( -\frac{2t}{\Delta t} + 1 \right), \quad (152)$$

where the time-dependent  $g(t)$  utilizes the compact mask function  $\Gamma_{[\text{erf};1]}$  to smoothly accelerate from  $g(0) = 0$  to  $g(\Delta t) = 1$  at  $\Delta t = 4$ , with steady uniform flow boundary conditions  $g(t > \Delta t) = 1$  until the end time  $t_{\text{end}} = 10$ . The inner coordinate singularity at  $r = 0$  is avoided by prescribing rotating no slip inner boundaries within the mask at  $r = R_1 = 1/10$ .

$$u(R_1) = 0, \quad v(R_1) = R_1 \Omega(t), \quad \text{where } \Omega(t) = \sin \left( \frac{2t}{\pi} \right). \quad (153)$$

where the cylinder angular velocity  $\Omega$  is sinusoidal. The reference numerical simulation simply replaces the volume penalization with the corresponding rotating no-slip boundary conditions applied at  $r = 1$ .

**Force calculations** — The most physically meaningful metrics of volume penalization accuracy are of force and torque accuracy. The force  $F_0$  and torque  $T_0$  on a no slip boundary are defined by surface integrals of the tangential and normal components of the stress tensor

$$F_{0,x} = \int_0^{2\pi} \left[ r \left( \cos \theta (-P + \frac{2}{\text{Re}} \partial_r u) - \sin \theta \frac{1}{\text{Re} r} (\partial_\theta u + r \partial_r v - v) \right) \right]_{r=R_1} d\theta, \quad (154)$$

$$F_{0,y} = \int_0^{2\pi} \left[ r \left( \sin \theta (-P + \frac{2}{\text{Re}} \partial_r u) + \cos \theta \frac{1}{\text{Re} r} (\partial_\theta u + r \partial_r v - v) \right) \right]_{r=R_1} d\theta, \quad (155)$$

$$T_0 = \int_0^{2\pi} \left[ \frac{r}{\text{Re}} (\partial_\theta u + r \partial_r v - v) \right]_{r=R_1} d\theta. \quad (156)$$

We note that both the true cylinder and the volume penalized cylinder possess no-slip boundaries (at  $r = 1$  and  $r = 1/10$  respectively), so this calculation is performed for both simulations. The volume penalized force  $F$  and torque  $T$  calculations involves a volume integral of the damping term, a correction from the stress on the interior no-slip cylinder, and a correction for the

rotational acceleration [37, 13],

$$F_x = \int_0^{2\pi} \int_{R_1}^{R_2} \frac{\Gamma}{\eta} (\cos \theta u - \sin \theta (v - r\Omega)) r dr d\theta + F_{0,x}, \quad (157)$$

$$F_y = \int_0^{2\pi} \int_{R_1}^{R_2} \frac{\Gamma}{\eta} (\sin \theta u + \cos \theta (v - r\Omega)) r dr d\theta + F_{0,y}, \quad (158)$$

$$T = \int_0^{2\pi} \int_{R_1}^{R_2} \frac{\Gamma}{\eta} (v - r\Omega) r^2 dr d\theta + \int_0^{2\pi} \int_{R_1}^1 \dot{\Omega} r^3 dr d\theta + T_0. \quad (159)$$

We note that the azimuthal symmetry of the acceleration correction implies it only appears in the torque calculation.

**Volume penalty parameters**— Three different types of penalty mask are chosen, corresponding to the choices

- $\Gamma_{0,0}$ : Standard discontinuous mask  $\ell = 0, \delta = 0$ ,
- $\Gamma_{\varepsilon,0}$ : Shifted discontinuous mask  $\ell = \varepsilon, \delta = 0$ ,
- $\Gamma_{0,\alpha\varepsilon}$ : Zero-shift smoothed mask  $\ell = 0, \delta = \alpha\varepsilon$ ,

where the smooth mask function is defined using a compactified error function

$$\Gamma_{\ell,\delta}(r) = \widehat{\Gamma}_{[\text{erf};1]} \left( \frac{r - 1 - \ell}{\delta} \right), \quad \text{where } \delta = 3.801719284432 \varepsilon. \quad (160)$$

We then examine these mask families for  $\eta_1 = 10^{-2}$ ,  $\eta_2 = 10^{-3}$ , and  $\eta_3 = 10^{-4}$ .

## 6.2 Numerical method and parameters

The initial value problem is simulated using the Dedalus framework [1]<sup>2</sup>. Dedalus is a general-purpose framework for solving partial differential equations using spectral methods. Dedalus allows users to construct domains from the direct product of spectral series including Fourier Series, Chebyshev polynomial series, and continuous segments of Chebyshev polynomials (a compound Chebyshev basis), and to enter systems of PDEs in plain text. The terms entered on the left-hand side (LHS) of the equations must be linear and are discretised into sparse and banded matrices acting on the spectral coefficients of the solution. Boundary conditions are enforced at the endpoints of the Chebyshev bases with the use of a preconditioned Chebyshev-tau method. The equations can be evolved using a range of mixed implicit-explicit timesteppers, with the LHS terms being integrated implicitly, and the right-hand side (RHS) terms being integrated explicitly. The framework is written in the Python programming language but utilizes compiled libraries for performance and automatically parallelizes the solvers using MPI, enabling for rapid prototyping and comparisons between models as well as efficient simulations at scale.

The test and reference solutions use well-resolved conformal cylindrical grids in Dedalus to investigate the mathematical error of the penalized problem for unsteady flow at moderate Reynolds number. The spatial discretisation consists of a Fourier basis using 512 modes for the azimuthal direction and Chebyshev bases in the radial direction. For the reference solution, a single Chebyshev domain is defined for the interval  $I = [1, R_2]$  and the surface boundary conditions are directly applied at the inner Chebyshev boundary, which coincides with the surface of the cylinder. For the penalized simulations, a compound Chebyshev basis is used with

<sup>2</sup>Visit the Dedalus home page at <http://dedalus-project.org/>.

additional segments resolving the transition of the mask and the interior of the cylinder. The compound Chebyshev segments consist of the intervals  $I_1 = [R_1, 1 + \ell - \delta]$ ,  $I_2 = [1 + \ell - \delta, 1 + \ell + \delta]$ , and  $I_3 = [1 + \ell + \delta, R_2]$ , where  $R_1 = 0.1$  and  $R_2 = 10$ . Each interval is discretised using 256 modes, 64 modes, and 256 modes respectively. In the singular case  $\delta = 0$  the middle interval is neglected.

The system is timestepped using a third order accurate backward difference scheme. We found other timesteppers (such as Crank-Nicolson Adams-Bashforth or Runge-Kutta schemes) performed poorly with time varying velocity boundary conditions during the acceleration phase  $t < 4$ . The backwards difference scheme was validated as converged by observing spectral accuracy ( $\mathcal{O}(10^{-10})$  error) for the pressure equation and boundary conditions at all times during the simulation. The penalty term is timestepped explicitly (for accuracy reasons [26]) with the stability constraint suggesting our choice of timestep  $5 \times 10^{-5}$ . This system is then timestepped uniformly up to time  $t = 10$  for all simulations.

Table 2: Table of fixed cylinder simulation parameters.

| Parameter           | Symbol     | Value |
|---------------------|------------|-------|
| Reynolds number     | Re         | 200   |
| Inner domain radius | $R_1$      | 0.1   |
| Outer domain radius | $R_2$      | 10    |
| Final time          | $t_{end}$  | 10    |
| Azimuthal modes     | $N_\theta$ | 512   |

Table 3: Table of varying cylinder simulation parameters.

| Simulation | $\ell$                | $\delta$              | $\eta$             | $\varepsilon$         |
|------------|-----------------------|-----------------------|--------------------|-----------------------|
| (0, 0)     | 0                     | 0                     | $1 \times 10^{-2}$ | $7.07 \times 10^{-3}$ |
| (0, 1)     | 0                     | 0                     | $1 \times 10^{-3}$ | $2.23 \times 10^{-3}$ |
| (0, 2)     | 0                     | 0                     | $1 \times 10^{-4}$ | $7.07 \times 10^{-4}$ |
| (1, 0)     | $7.07 \times 10^{-2}$ | 0                     | $1 \times 10^{-2}$ | $7.07 \times 10^{-2}$ |
| (1, 1)     | $7.07 \times 10^{-3}$ | 0                     | $1 \times 10^{-3}$ | $2.23 \times 10^{-3}$ |
| (1, 2)     | $7.07 \times 10^{-4}$ | 0                     | $1 \times 10^{-4}$ | $7.07 \times 10^{-4}$ |
| (2, 0)     | 0                     | $2.69 \times 10^{-2}$ | $1 \times 10^{-2}$ | $7.07 \times 10^{-2}$ |
| (2, 1)     | 0                     | $8.50 \times 10^{-3}$ | $1 \times 10^{-3}$ | $2.23 \times 10^{-3}$ |
| (2, 2)     | 0                     | $2.69 \times 10^{-3}$ | $1 \times 10^{-4}$ | $7.07 \times 10^{-4}$ |

### 6.3 Richardson extrapolation

A general technique to accelerate convergence of sequences with known asymptotic behaviour is *Richardson extrapolation*. Specifically, for a quantity  $X_i, X_j$  derived from simulations with penalty parameters  $\eta_j$  and  $\eta_k$  we can calculate an *extrapolated* quantity  $\bar{X}_{ij}$  as

$$\bar{X}_{ij} \equiv \frac{X_i/\eta_i - X_j/\eta_j}{1/\eta_i - 1/\eta_j}. \quad (161)$$

Assuming the quantities  $X_i, X_j$  obey identical leading order behaviour proportional to  $\eta$ , the extrapolated sum  $\bar{X}_{ij}$  will subtract out this leading order error. Hence at the small added cost of a lower resolution simulation at larger  $\eta$ , one can achieve  $\mathcal{O}(\eta^2)$  accuracy in practice.

## 6.4 Summary of errors

Figure 8 compares the pressure  $P$  and vorticity  $\omega_z$  fields for the reference simulation and the volume penalty simulation (2, 2). Snapshots are shown every two seconds until time  $t = 10$ , and a black dot illustrates the oscillation of the cylinder. The pressure color scale is calibrated to the steady state uniform flow after  $t = 4$ , and is saturated initially ( $t = 0$ , where  $P = 0$ ) and at the period of maximum acceleration ( $t = 2$ ), where a large pressure drop of order 20 is induced over the domain. The figures are plotted to a radius of  $r = 8$  to capture the vortex evolution. After  $t = 4$  the outer boundary conditions are steady and higher pressures are visible at the leading edge of the cylinder, with low pressure zones around the vortices and the sides of the cylinder. The pressure varies within the volume penalized cylinder, and so the force on the inner no-slip boundary must be accounted for in the drag calculation. Vortex shedding is observed immediately due to the rotation of the cylinder (in addition to the inherent instability of the von Karman vortex street). No visual difference is observable between the simulations, so a more delicate comparison must be shown.

Figure 9 plots the pointwise error  $u - u_0$  in the radial velocity field at the final timestep  $t = 10$  for the different mask choices ( $\Gamma_{0,0}, \Gamma_{\ell,0}, \Gamma_{0,\delta}$ ) and penalty choices  $\eta = \eta_0, \eta_1, \eta_2$ . The colormap range is normalized to half the maximum local error  $\mathcal{E}_\infty$  to indicate shape, and the numerical value  $\mathcal{E}_\infty$  is printed below to indicate amplitude. We see optimal adjustments lead to identical spatial profiles of the error (in the two right columns), with the amplitude decreasing as  $\mathcal{O}(\eta)$ . This is a visual demonstration of the  $\mathcal{O}(\eta)$  convergence in the flow for the optimized masks. The error for the standard discontinuous mask lacks this property, varying in both amplitude and pattern with  $\eta$ , implying a different convergence rate (namely as  $\mathcal{O}(\sqrt{\eta}) \propto \mathcal{O}(\varepsilon)$ ). This is strong empirical evidence for the validity of the asymptotic expansions of section 4.

This also motivates investigation of extrapolated calculations in fig. 9. Two extrapolations were performed for each mask, using consecutive values of  $\eta_0, \eta_1$ , and  $\eta_1, \eta_2$ . No performance improvement is observed for the standard discontinuous mask. This is expected – the leading order  $\mathcal{O}(\varepsilon)$  displacement length implies a standard mask does not possess the  $\mathcal{O}(\eta)$  convergence required to apply successful Richardson extrapolation. However marked improvements are observed for extrapolations of the *optimized* masks. Extrapolation using  $\eta_0 = 10^{-2}$  and  $\eta_1^{-3}$  is able to achieve an accuracy commensurate with  $\eta_2 = 10^{-4}$ , and extrapolation using  $\eta_1$  and  $\eta_2$  is almost two orders of magnitude more accurate than for  $\eta_2$  alone. The reduction in  $\mathcal{E}_\infty$  by two orders of magnitude (from  $\approx 3 \times 10^{-3}$  to  $3 \times 10^{-5}$ ) implies  $\mathcal{O}(\eta^2)$  convergence for Richardson extrapolations of optimal masks. This is a massive performance boost. By running a smaller second simulation in tandem with the first, it is possible to improve the convergence to  $\mathcal{O}(\eta^2) \propto \mathcal{O}(\varepsilon^4)$ , implying the *computational effort* to halve the error is only  $2^{(D+2)/4}$  in  $D$  dimensions – It only takes twice the effort to halve the error in two dimensions, and slightly more than that in three dimensions, vastly more efficient than the 16 and 32 times scaling for the uncorrected volume penalty mask. We note that this extrapolation is here performed as a post-processing procedure, but could equally be calculated during a simulation run. The inherent Lyapunov time scale of chaotic fluid flows would require reinitializing each simulation over this order of time steps to prevent the two simulations drifting out of synchronization.

We then calculate the global and local error norms at the final timestep for the radial velocity  $u$ , the azimuthal velocity  $v$ , the true pressure  $P$ , and the true vorticity  $\omega_z$  in fig. 10. Several trends are apparent from this plot. Foremost, we see different performance between the different penalization approaches. The standard discontinuous mask  $\Gamma_{0,0}$  (black) performs significantly worse than the optimized masks, tending to the predicted  $\mathcal{O}(\eta^{1/2})$  convergence rate. Optimized masks instead show almost exact  $\mathcal{O}(\eta)$  convergence, while the Richardson extrapolated predictions are even more efficient, with  $\mathcal{O}(\eta^2)$  error (based off the smallest  $\eta$  used). However, for the smallest penalization  $\eta_0 = 1 \times 10^{-2}$ , we see that all approaches are equally accurate; In the intermediate damping regime, the dominant error is not due to the

displacement length (which we are able to correct with optimized masks), but *time scale* errors due to interior pressure gradients and acceleration of the penalty mask, as seen for stagnation point flow in section 5. Similar behaviour for the global error is observed for the azimuthal velocity  $v$  and pressure  $P$ .

The differing behaviour of the global  $\mathcal{E}_1$  and local  $\mathcal{E}_\infty$  errors can be interpreted by considering the regularity of the penalized and ‘‘ideal’’ solutions for each variable. A discontinuous mask function implies the velocity is  $C^1$ , and the pressure is  $C^0$ , while a smooth mask function implies smooth solutions. However, the ideal solutions are less regular. The radial velocity has zero value and derivative at the boundary, so is also  $C^1$  differentiable. This can be uniformly approximated by the  $C^1$  or  $C^\infty$  volume penalized solution, leading to identical scaling of global  $\mathcal{E}_1$  and local  $\mathcal{E}_\infty$  errors – there is no localization of error.

The *reference* azimuthal velocity  $v_0$  and pressure  $p_0$  however exhibit a kink at the boundary – they are only  $C^0$  and possess an  $\mathcal{O}(1)$  jump in the derivative (compare the ideal and penalized velocities in fig. 4). This is less regular than the volume penalized solution, hence there must be  $\mathcal{O}(\varepsilon)$  disagreement between the ‘ideal’ and penalized solutions in the boundary region. We are essentially trying to fit a corner with a smooth function of curvature  $\varepsilon$ . By calibrating the mask and eliminating the displacement length, it is possible to localize this  $\mathcal{O}(\varepsilon)$  error to the  $\mathcal{O}(\varepsilon)$  boundary region, implying a local error at the boundary of  $\mathcal{O}(\varepsilon)$ , but a global error of only  $\mathcal{O}(\varepsilon^2)$  for the tangential velocity and pressure.

The derivative (vorticity) is even less regular – it is *discontinuous* at the boundary. Hence there must be  $\mathcal{O}(1)$  disagreement in the interior of the mask near the boundary. If extended into the fluid for the optimal masks, this gives  $\mathcal{O}(1)$  local error  $\mathcal{E}_\infty$ , but only  $\mathcal{O}(\varepsilon)$  local error (due to displacement length) for the unshifted mask. This implies identical global error scaling of  $\mathcal{E}_1 = \mathcal{O}(\varepsilon)$  – the standard mask generates  $\mathcal{O}(\varepsilon)$  error throughout the domain, while the calibrated masks generate  $\mathcal{O}(1)$  error in the  $\mathcal{O}(\varepsilon)$  boundary region, and  $\mathcal{O}(\varepsilon^2)$  error elsewhere.

We finally examine the most physically relevant metrics of accuracy – the drag  $\Delta F$  and torque  $\Delta T$  errors. We plot time series of the reference horizontal drag  $F_{0,x}$ , vertical lift  $F_{0,y}$ , and reference torque  $T_0$  are in fig. 11. Heightened drag is observed during the peak fluid acceleration ( $t < \Delta t = 4$ ), corresponding to the large induced pressure gradient observed at  $t = 2$  in fig. 11. A significant lift force is also generated during the simulation, as expected from the Magnus effect [30].

Figure 12 compares the time series of the horizontal drag error  $\Delta F_x$ , vertical drag error  $\Delta F_y$ , and torque error  $\Delta T$  for each choice of mask  $\Gamma_{0,0}, \Gamma_{\ell,0}$  and  $\Gamma_{0,\delta}$  and choice of damping  $\eta = \eta_0, \eta_1, \eta_2$ . All the masks improve similarly in the transition from  $\eta_1 = 10^{-2}$  to  $\eta_2 = 10^{-3}$ , in keeping with the intermediate damping regime. However, after this point, completely different behaviour is apparent. The unshifted discontinuous mask  $\Gamma_{0,0}$  shows a transition from  $\mathcal{O}(\text{Re } \varepsilon^2)$  to  $\mathcal{O}(\varepsilon)$  convergence after  $\eta = 10^{-2}$ , whereas the optimized masks each maintain consistent  $\mathcal{O}(\eta)$  convergence. The temporal profile of the error is largely identical for the corrected masks, but inconsistent for the unshifted discontinuous mask.

We can also apply the extrapolation procedure to the drag, lift and torque calculations, and we find similar performance improvements. No improvement occurs for the standard mask, while the adjusted masks each achieve much greater accuracy. Decreasing  $\eta$  by a factor of 10 improves the extrapolated error by a factor of 100 – again implying  $\mathcal{O}(\eta^2)$  error. This is an extraordinary improvement in the accuracy of the volume penalty method, attaining drag errors of order  $10^{-5}$  using extrapolation at  $\eta = 10^{-4}$ .

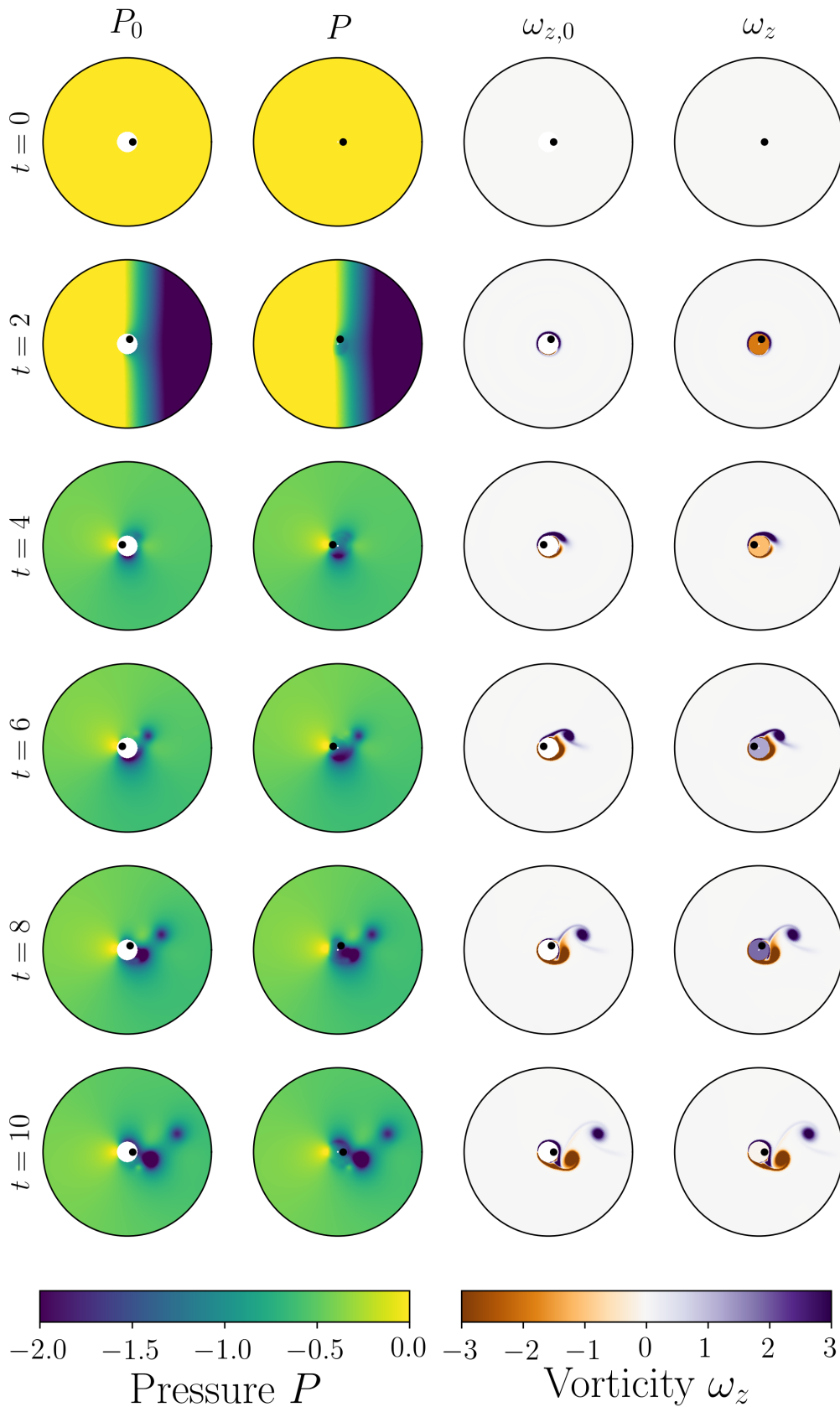


Figure 8: Time snapshots of pressure  $P = p - (u^2 + v^2)/2$ , and vorticity  $\omega_z = q/r$  for the reference and (2,2) volume penalty cylinder simulations. The interior black dot shows the orientation of the rotating cylinder. Rotation of the volume penalized cylinder results in non-zero vorticity within the object (column 4). The pressure and vorticity fields are indistinguishable outside the object however.

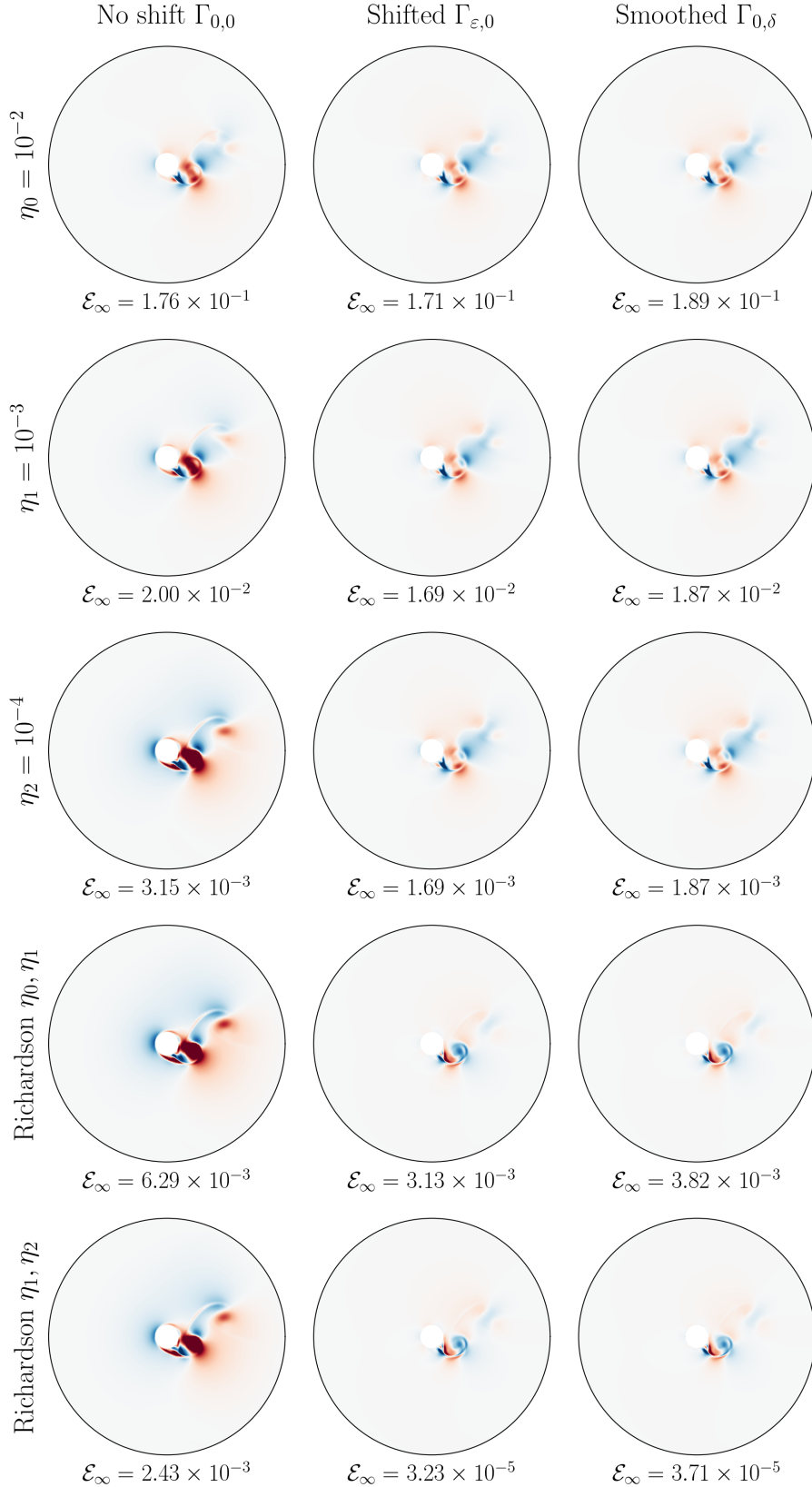


Figure 9: Error pattern between penalised and reference radial velocities  $u - u_0$ . Plots are made at  $t = 10$  for the three different mask choices, at three choices of  $\eta$ . Each color map is normalized to the maximum error of the velocity field  $\mathcal{E}_\infty$ . The spatial pattern of the error is almost identical for all optimized masks, and differs only in the magnitude as  $\eta$  is decreased. Two Richardson extrapolated fields are calculated for each mask type, which significantly improve the error for the optimized masks, but fails for the unoptimized mask.

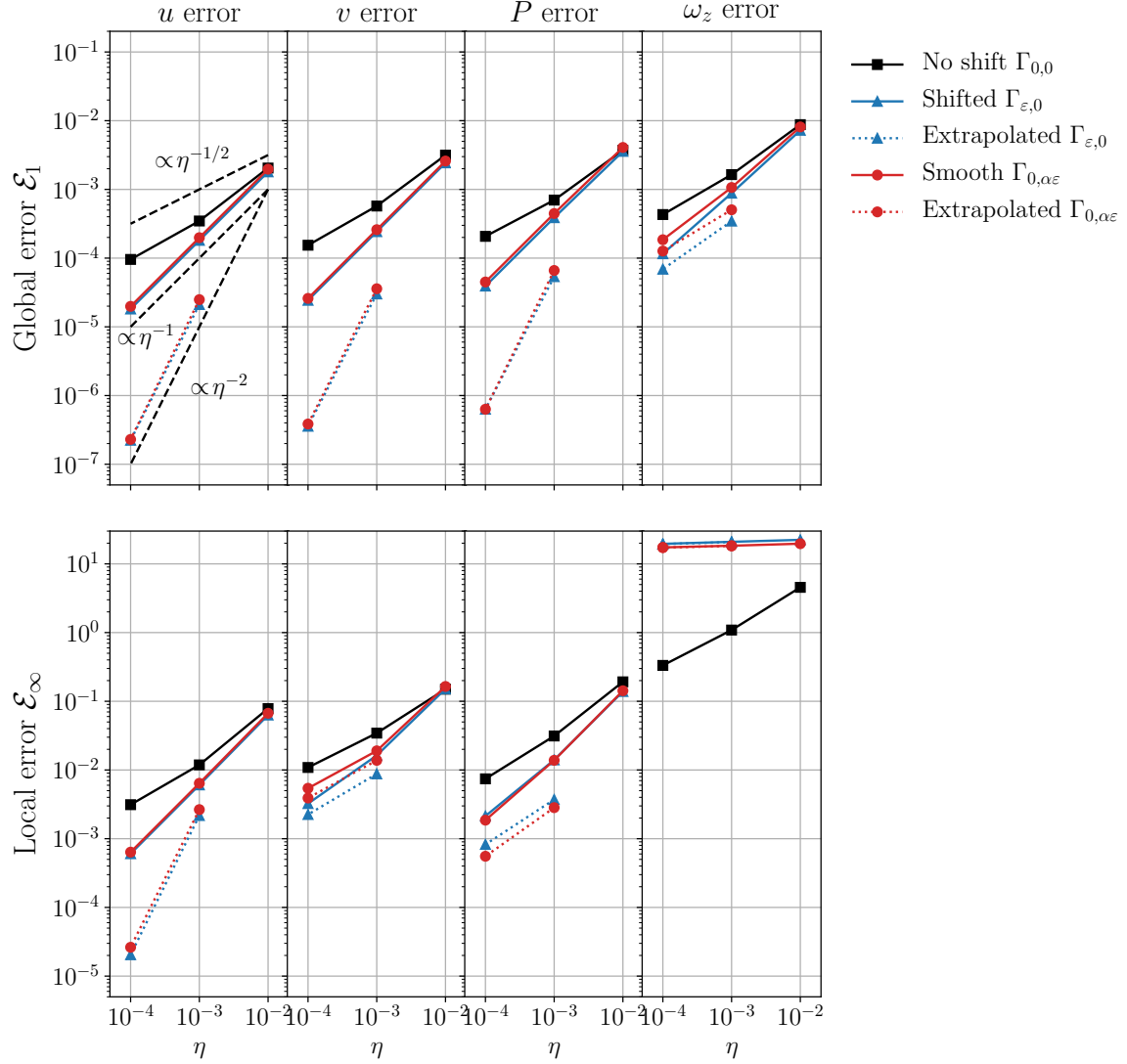


Figure 10: Plots of the global  $\mathcal{E}_1$  and local error  $\mathcal{E}_\infty$  for  $u, v, P$ , and  $\omega_z$  as a function of  $\eta$ , for three mask choices ( $\Gamma_{0,0}$  (black),  $\Gamma_{\varepsilon,0}$  (blue),  $\Gamma_{0,\delta}$  (red)). Errors were calculated for  $1 < r < 10$  at  $t = 10$ . Extrapolated calculations are dotted. Different convergence behaviours are apparent for different variables and different masks.

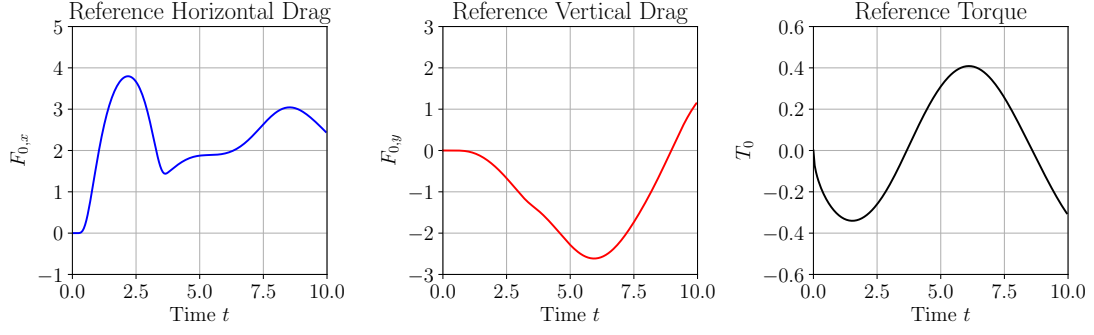


Figure 11: Time series of the total horizontal drag  $F_{0,x}$ , total vertical drag  $F_{0,y}$ , and total torque  $T_0$  for the reference cylinder simulation at  $Re = 200$ .

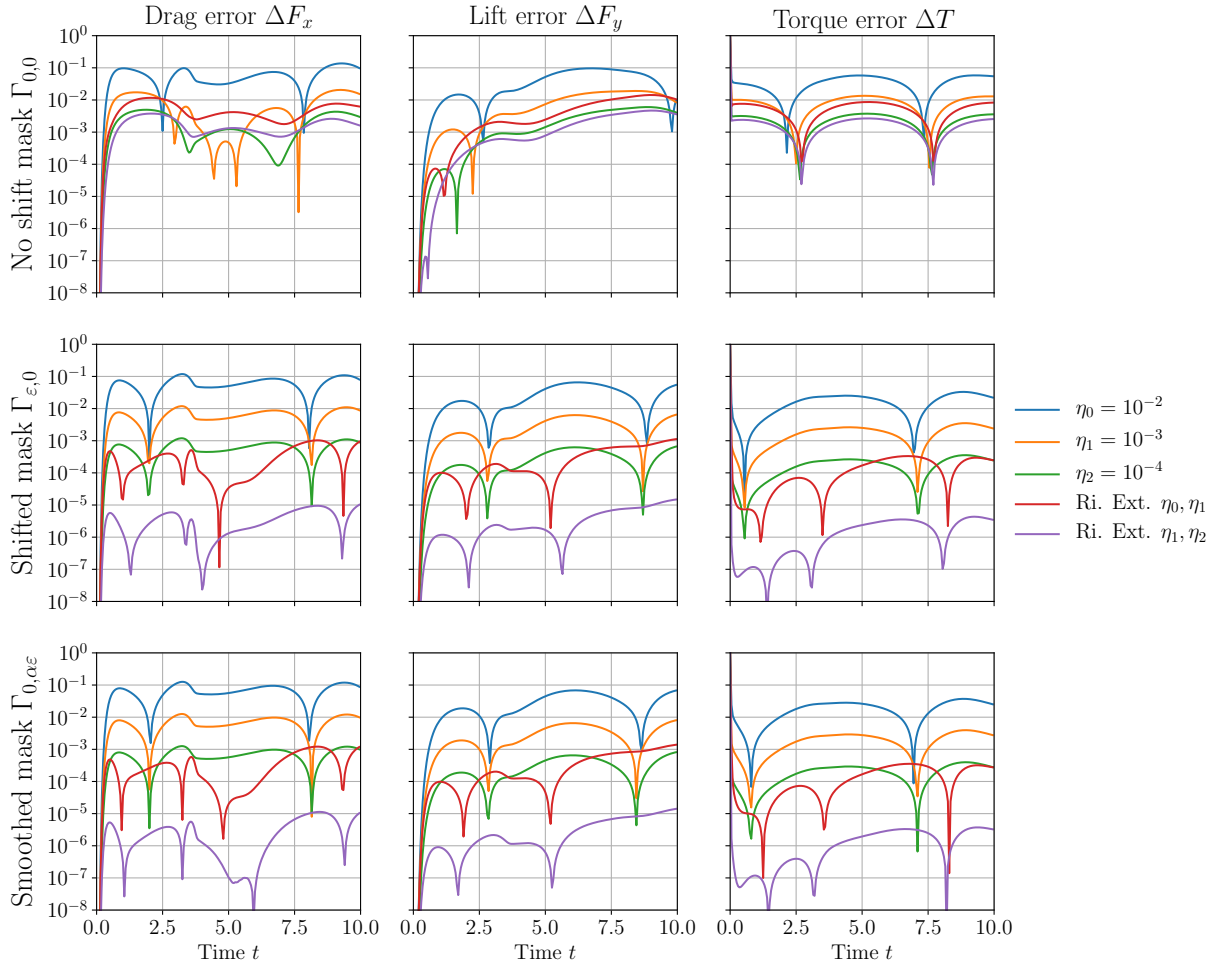


Figure 12: Time series of the drag error  $\Delta F_x$ , lift error  $\Delta F_y$ , and torque error  $\Delta T$  at  $Re = 200$  for standard discontinuous  $\Gamma_{0,0}$ , optimal shifted  $\Gamma_{\epsilon,0}$ , and optimal smooth  $\Gamma_{0,\alpha\epsilon}$  masks for different choices of damping  $\eta = 10^{-2}, 10^{-3}, 10^{-4}$ , and extrapolated errors.

## 7 Conclusions

- The volume penalty method approximates Dirichlet boundary conditions using strong linear damping.
- The damping induces a penalization *time* scale  $\eta$ , and penalization *length* scale  $\varepsilon$ , which are related via the Reynolds number  $\eta = \text{Re} \varepsilon^2$ .
- The error in the fluid is in general  $\mathcal{O}(\varepsilon)$  due to the *displacement length* of general mask functions  $\Gamma$ .
- The displacement error can be eliminated by *shifting* and *smoothing* the mask near the boundary.
- This calculation can be done once efficiently using a *Riccati* transformation.
- The time scale error results from pressure gradients within the solid, and is proportional to  $\text{Re} \varepsilon^2 = \eta$ . This leads to two damping regimes for large  $\text{Re}$ .
- *Intermediate* damping  $1 > \eta > \varepsilon > \text{Re}^{-1}$  implies the ‘second order’ time scale error dominates the ‘first order’ displacement length error, giving heightened convergence.
- For *strong* damping  $1 > \text{Re}^{-1} > \varepsilon > \eta$  the displacement length error dominates and mask corrections must be used to achieve  $\mathcal{O}(\varepsilon^2)$  accuracy.
- At small Reynolds number  $\text{Re} < 1$ , the intermediate damping regime disappears, and zero-displacement length masks must be used to achieve  $\mathcal{O}(\varepsilon^2)$  accuracy.
- The accuracy of the force and torque calculations are proportional to the accuracy of the flow field. Optimized masks allow  $\mathcal{O}(\varepsilon^2)$  accurate drag calculations.
- The comparison of the damping length and time scale with the turbulent Kolmogorov length scale and CFL time scale imply multiple regimes for *computational cost* at large  $\text{Re}$ .
- $\eta > \text{Re}^{-1/2}$  implies the turbulence length and time scale are finer than the damping length and time scale. Volume penalized boundaries can be added for no extra computational cost with error  $\eta = \text{Re}^{-1/2}$ .
- Richardson extrapolation can be used on optimized masks to boost error convergence to  $\mathcal{O}(\eta^2)$ .

We discovered these findings using a straightforward multiple scales matched asymptotics procedure based off the signed distance function coordinate system. We first validated these prescriptions in two simple problems with analytic solutions, Poiseuille, and viscous stagnation point flow. Stagnation point flow is a minimal example of the regime splitting at second order. We then verified these findings by simulating accelerating flow past a rotating cylinder at  $\text{Re} = 200$ .

### 7.1 Further directions

We have now derived the maths necessary to address the asymptotic convergence of similar vector valued equations. We wish to apply these methods to derive higher order accurate models of coupled convection and melting and dissolution using the phase field method [23, 8, 12]. The ultimate goal is a unified set of second-order accurate methods to enforce arbitrary geometry boundary conditions of arbitrary type.

## Acknowledgments

Eric Hester acknowledges support from The University of Sydney through the Postgraduate Teaching Fellowship, and the Phillip Hofflin International Research Travel Scholarship. Geoffrey Vasil acknowledges support from the Australian Research Council, project number DE140101960. The authors would also like to acknowledge the thoughtful input from many discussions with Daniel Lecoanet, Chris Lustri, Benjamin Favier, Laurent Duchamin, and Kai Schneider.

## References

- [1] ASCL.net - Dedalus: Flexible framework for spectrally solving differential equations. <http://ascl.net/1603.015>.
- [2] D. M. Anderson, G. B. McFadden, and A. A. Wheeler. Diffuse-Interface Methods in Fluid Mechanics. *Annual Review of Fluid Mechanics*, 30(1):139–165, 1998.
- [3] P. Angot. Analysis of singular perturbations on the Brinkman problem for fictitious domain models of viscous flows. *Mathematical Methods in the Applied Sciences*, 22(16):1395–1412, Nov. 1999.
- [4] P. Angot, C.-H. Bruneau, and P. Fabrie. A penalization method to take into account obstacles in incompressible viscous flows. *Numerische Mathematik*, 81(4):497–520, Feb. 1999.
- [5] J. P. Boyd. Fourier embedded domain methods: Extending a function defined on an irregular region to a rectangle so that the extension is spatially periodic and  $C^\infty$ . *Applied Mathematics and Computation*, 161(2):591–597, Feb. 2005.
- [6] M. Briscolini and P. Santangelo. Development of the mask method for incompressible unsteady flows. *Journal of Computational Physics*, 84(1):57–75, Sept. 1989.
- [7] M. Burger, O. L. Elvetun, and M. Schlottbom. Analysis of the Diffuse Domain Method for Second Order Elliptic Boundary Value Problems. *Foundations of Computational Mathematics*, 17(3):627–674, June 2017.
- [8] G. Caginalp and X. Chen. Convergence of the phase field model to its sharp interface limits. *European Journal of Applied Mathematics*, 9(4):417–445, Aug. 1998.
- [9] J. W. Cahn and J. E. Hilliard. Free Energy of a Nonuniform System. I. Interfacial Free Energy. *The Journal of Chemical Physics*, 28(2):258–267, Feb. 1958.
- [10] G. Carbou and P. Fabrie. Boundary layer for a penalization method for viscous incompressible flow. *Advances in Differential Equations*, 8(12):1453–1480, 2003.
- [11] J. D. COLE. ON A QUASI-LINEAR PARABOLIC EQUATION OCCURRING IN AERODYNAMICS. *Quarterly of Applied Mathematics*, 9(3):225–236, 1951.
- [12] C. Eck, G. Caginalp, and X. Chen. A rapidly converging phase field model. *Discrete and Continuous Dynamical Systems*, 15(4):1017–1034, May 2006.
- [13] T. Engels, D. Kolomenskiy, K. Schneider, and J. Sesterhenn. Numerical simulation of fluid–structure interaction with the volume penalization method. *Journal of Computational Physics*, 281(Supplement C):96–115, Jan. 2015.

- [14] T. Engels, D. Kolomenskiy, K. Schneider, and J. Sesterhenn. FluSI: A Novel Parallel Simulation Tool for Flapping Insect Flight Using a Fourier Method with Volume Penalization. *SIAM Journal on Scientific Computing*, 38(5):S3–S24, Jan. 2016.
- [15] S. Franz, H.-G. Roos, R. Gärtner, and A. Voigt. A Note on the Convergence Analysis of a Diffuse-domain Approach. *Computational Methods in Applied Mathematics*, 12(2), 2012.
- [16] J. W. Gibbs. On the equilibrium of heterogeneous substances. *American Journal of Science*, Series 3 Vol. 16(96):441–458, Jan. 1878.
- [17] D. Goldstein, R. Handler, and L. Sirovich. Modeling a No-Slip Flow Boundary with an External Force Field. *Journal of Computational Physics*, 105(2):354–366, Apr. 1993.
- [18] P. C. Hohenberg and B. I. Halperin. Theory of dynamic critical phenomena. *Reviews of Modern Physics*, 49(3):435–479, July 1977.
- [19] E. Hopf. The partial differential equation  $u_t + uux = Mxx$ . *Communications on Pure and Applied Mathematics*, 3(3):201–230, 1950.
- [20] G. Iaccarino and R. Verzicco. Immersed boundary technique for turbulent flow simulations. *Applied Mechanics Reviews*, 56(3):331–347, May 2003.
- [21] D. Jacqmin. Calculation of Two-Phase Navier–Stokes Flows Using Phase-Field Modeling. *Journal of Computational Physics*, 155(1):96–127, Oct. 1999.
- [22] B. Kadoch, D. Kolomenskiy, P. Angot, and K. Schneider. A volume penalization method for incompressible flows and scalar advection–diffusion with moving obstacles. *Journal of Computational Physics*, 231(12):4365–4383, June 2012.
- [23] A. Karma and W.-J. Rappel. Quantitative phase-field modeling of dendritic growth in two and three dimensions. *Physical Review E*, 57(4):4323–4349, Apr. 1998.
- [24] N. K. R. Kevlahan and J.-M. Ghidaglia. Computation of turbulent flow past an array of cylinders using a spectral method with Brinkman penalization. *European Journal of Mechanics - B/Fluids*, 20(3):333–350, May 2001.
- [25] K. Khadra, P. Angot, S. Parneix, and J.-P. Caltagirone. Fictitious domain approach for numerical modelling of Navier–Stokes equations. *International Journal for Numerical Methods in Fluids*, 34(8):651–684, Dec. 2000.
- [26] D. Kolomenskiy and K. Schneider. A Fourier spectral method for the Navier–Stokes equations with volume penalization for moving solid obstacles. *Journal of Computational Physics*, 228(16):5687–5709, Sept. 2009.
- [27] J. S. Langer. MODELS OF PATTERN FORMATION IN FIRST-ORDER PHASE TRANSITIONS. In *Directions in Condensed Matter Physics*, pages 165–186. 1986.
- [28] K. Y. Lervåg and J. Lowengrub. Analysis of the diffuse-domain method for solving PDEs in complex geometries. *Communications in Mathematical Sciences*, 13(6):1473–1500, 2015.
- [29] X. Li, J. Lowengrub, A. Ratz, and A. Voigt. Solving PDEs in complex geometries: A diffuse domain approach. *Communications in mathematical sciences*, 7(1):81–107, Mar. 2009.
- [30] G. Magnus. Ueber die Abweichung der Geschosse, und: Ueber eine auffallende Erscheinung bei rotirenden Körpern. *Annalen der Physik*, 164(1):1–29, 1853.

- [31] R. Mittal and G. Iaccarino. Immersed Boundary Methods. *Annual Review of Fluid Mechanics*, 37(1):239–261, 2005.
- [32] C. S. Peskin. Numerical analysis of blood flow in the heart. *Journal of Computational Physics*, 25(3):220–252, Nov. 1977.
- [33] C. S. Peskin. The immersed boundary method. *Acta Numerica*, 11:479–517, Jan. 2002.
- [34] K. Schneider. Immersed boundary methods for numerical simulation of confined fluid and plasma turbulence in complex geometries: A review. *Journal of Plasma Physics*, 81(6), Dec. 2015.
- [35] K. Schneider, S. Neffaa, and W. J. T. Bos. A pseudo-spectral method with volume penalisation for magnetohydrodynamic turbulence in confined domains. *Computer Physics Communications*, 182(1):2–7, Jan. 2011.
- [36] J. Stefan. Ueber die Theorie der Eisbildung, insbesondere über die Eisbildung im Polarmeere. *Annalen der Physik*, 278(2):269–286, 1891.
- [37] M. Uhlmann. An immersed boundary method with direct forcing for the simulation of particulate flows. *Journal of Computational Physics*, 209(2):448–476, Nov. 2005.
- [38] J. D. van der Waals. The thermodynamic theory of capillarity under the hypothesis of a continuous variation of density. *Journal of Statistical Physics*, 20(2):200–244, Feb. 1979.
- [39] R. N. van Yen, D. Kolomenskiy, and K. Schneider. Approximation of the Laplace and Stokes operators with Dirichlet boundary conditions through volume penalization: A spectral viewpoint. *Numerische Mathematik*, 128(2):301–338, Oct. 2014.